

AD-A101 079 STANFORD UNIV CALIF DEPT OF AERONAUTICS AND ASTRONAUTICS F/G 17/7  
MODELING A CRYOGENIC HE3 NUCLEAR GYRO.(U)  
DEC 80 G L SHAW F49620-78-C-0088  
UNCLASSIFIED SUGAAR-525 AFOSR-TR-81-0523 ML

| OF |  
AD  
A101079

END  
DATE  
FILMED  
7-81  
DTIC

150 AFOSR-TR. 81-0523

(A)

Department of AERONAUTICS and ASTRONAUTICS  
STANFORD UNIVERSITY

SUDAAR 524

LEVEL 1

AD A101079

# MODELING A CRYOGENIC $\text{HE}^3$ NUCLEAR GYRO

by

Gerald L. Shaw

Department of Aeronautics and Astronautics  
Guidance and Control Laboratory  
and the  
Department of Physics

STANFORD UNIVERSITY  
Stanford, California 94305

DTIC  
ELECTE  
JUL 7 1981  
S D C

This research was supported by  
U.S. Air Force Institute of Technology  
Wright Patterson Air Force Base, Ohio 45433

with partial support from  
U.S. Office of Scientific Research  
Contract F-49620-78-C-0088

December 1980

Approved for public release  
distribution unlimited.

81 7 06 030

UNCLASSIFIED

SECURITY CLASSIFICATION OF THIS PAGE (When Data Entered)

| REPORT DOCUMENTATION PAGE   |  | READ INSTRUCTIONS<br>BEFORE COMPLETING FORM   |
|---|--|---|
| 1. REPORT NUMBER<br><b>AFOSR-TR-81-0523</b>   | 2. GOVT ACCESSION NO.<br><b>AD-A101079</b> | 3. RECIPIENT'S CATALOG NUMBER   |
| 4. TITLE (and Subtitle)<br><b>MODELING A CRYOGENIC HE<sup>3</sup> NUCLEAR GYRO</b>  |  | 5. TYPE OF REPORT & PERIOD COVERED<br><b>Scientific / INTERIM</b>                       |
|   |  | 6. PERFORMING ORG. REPORT NUMBER  |
| 7. AUTHOR(s)<br><b>Gerald L. Shaw</b>   |  | 8. CONTRACT OR GRANT NUMBER(s)<br><b>F49620-78-C-0088</b>                               |
| 9. PERFORMING ORGANIZATION NAME AND ADDRESS<br><b>Dept. of Aeronautics and Astronautics<br/>Stanford University<br/>Stanford, CA 94305</b>  |  | 10. PROGRAM ELEMENT, PROJECT, TASK<br>AREA & WORK UNIT NUMBERS<br><b>61102F 2301/A5</b> |
| 11. CONTROLLING OFFICE NAME AND ADDRESS<br><b>AFOSR/NP<br/>Bolling AFB<br/>Wash DC 20332</b>  |  | 12. REPORT DATE<br><b>Dec 1980</b>  |
|   |  | 13. NUMBER OF PAGES<br><b>89</b>  |
| 14. MONITORING AGENCY NAME & ADDRESS (if different from Controlling Office)<br><b>DAAG-05</b>   |  | 15. SECURITY CLASS. (of this report)<br><b>unclassified</b>                             |
|   |  | 15a. DECLASSIFICATION DOWNGRADING<br>SCHEDULE   |
| 16. DISTRIBUTION STATEMENT (of this Report)<br><br><b>Approved for public release;<br/>distribution unlimited.</b>  |  |   |
| 17. DISTRIBUTION STATEMENT (of the abstract entered in Block 20, if different from Report)  |  |   |
| 18. SUPPLEMENTARY NOTES   |  |   |
| 19. KEY WORDS (Continue on reverse side if necessary and identify by block number)  |  |   |
| 20. ABSTRACT (Continue on reverse side if necessary and identify by block number)<br>Over the last two decades, several nonconventional gyro schemes have been proposed. Directed primarily at eliminating the bearing problems in conventional mechanical gyros, it was anticipated that either better performance could be achieved or performance comparable to conventional gyros could be achieved at a lower cost. No attempt is made here to compare or contrast all of these various schemes, but rather to look at certain aspects of a particular device, a cryogenic He(3) nuclear gyro, and to provide models for estimating its performance. The nuclear gyro is highly dependent upon the stability and |  |   |

DD FORM 1473

1 JAN 73

EDITION OF 1 NOV 65 IS OBSOLETE

UNCLASSIFIED

SECURITY CLASSIFICATION OF THIS PAGE (When Data Entered)

UNCLASSIFIED

SECURITY CLASSIFICATION OF THIS PAGE(When Data Entered)

homogeneity of the magnetic field environment. A combination of low temperature physics technologies makes such a device practical. By generating the applied field with superconducting coils the stability of the field is guaranteed by the inherent stability of the persistent super-currents in these coils. Then protection from a changing external environment is provided by enclosing the device within a superconducting shield. Nevertheless, even in an ideal magnetic field environment, the nuclear gyro is subject to various rectification mechanisms. Of particular interest is the role kinematic rectification plays in this device. Rectification mechanisms are discussed, and mathematical models derived for calculating the methods of kinematic rectification drift. An experiment designed to measure and distinguish the kinematic rectification effects are discussed. The effects of thermal gradients and accelerations in the presence of an inhomogeneous magnetic field are also discussed, and models derived from which their magnitudes are calculated.

UNCLASSIFIED

SECURITY CLASSIFICATION OF THIS PAGE(When Data Entered)

C

SUDAAR 524

MODELING A CRYOGENIC  $\text{HE}^3$  NUCLEAR GYRO

by  
Gerald L. Shaw

DTIC  
ELECTE  
JUL 7 1981  
C

Department of Aeronautics and Astronautics  
Guidance and Control Laboratory  
and the  
Department of Physics  
STANFORD UNIVERSITY  
Stanford, California 94305

This research was supported by  
U.S. Air Force Institute of Technology  
Wright Patterson Air Force Base, Ohio 45433

with partial support from  
U.S. Office of Scientific Research  
Contract F-49620-78-C-0088

AIR FORCE OFFICE OF SCIENTIFIC RESEARCH (AFSC)  
NOTICE OF TRANSMITTAL TO DDC  
This technical report has been reviewed and is  
approved for public release IAW AFR 130-12 (7b).  
Distribution is unlimited.  
A. D. KLOSE  
Technical Information Officer

December 1980

## ABSTRACT

Over the last two decades, several nonconventional gyro schemes have been proposed. Directed primarily at eliminating the bearing problems in conventional mechanical gyros, it was anticipated that either better performance could be achieved or performance comparable to conventional gyros could be achieved at a lower cost. No attempt is made here to compare or contrast all of these various schemes, but rather to look at certain aspects of a particular device, a cryogenic  $\text{He}^3$  nuclear gyro, and to provide models for estimating its performance.

The nuclear gyro is highly dependent upon the stability and homogeneity of the magnetic field environment. A combination of low temperature physics technologies makes such a device practical. By generating the applied field with superconducting coils the stability of this field is guaranteed by the inherent stability of the persistent supercurrents in these coils. Then protection from a changing external environment is provided by enclosing the device within a superconducting shield.

Nevertheless, even in an ideal magnetic field environment, the nuclear gyro is subject to various rectification mechanisms. Of particular interest is the role kinematic rectification plays in this device. Rectification mechanisms are discussed, and mathematical models derived for calculating the methods of kinematic rectification drift. An experiment designed to measure and distinguish the kinematic rectification effects are discussed.

The effects of thermal gradients and accelerations in the presence of an inhomogeneous magnetic field are also discussed, and models derived from which their magnitudes are calculated.

|               |                    |
|---------------|--------------------|
| Accession For |                    |
| NTIS          | GR&I               |
| DTIC TAB      |                    |
| Unannounced   |                    |
| Justification |                    |
| By            | Distribution/      |
| Dist          | Availability Codes |
|               | Avail and/or       |
|               | Special            |

#### ACKNOWLEDGMENTS

I would like first to thank my advisor, Professor Daniel B. DeBra, for his advice and encouragement throughout this research and indeed throughout my years here at Stanford University. I would also like to thank Professor William Fairbank who, together with Professor DeBra, directed this research.

I wish to thank Professors Bershader and Cannon for their critical reading of this dissertation.

I would also like to thank the United States Air Force's Air Force Institute of Technology for supporting me throughout this program. Special appreciation is extended to Capt. Sam Brown, my program manager for most of my stay.

I would especially like to thank Drs. Mike Taber and Blas Cabrera for their helpful suggestions, patience, and generous provision of time.

Special thanks are also due Jim Nelson and Joe Ascorra for their excellent machine work on the Macor gyro; and to Ms. Ida M. Lee for her expert typing and editing.

I am forever indebted to my wife, Nancy, for her unending encouragement and unselfish sacrifice, which has made this work not just possible but enjoyable as well. Also, thanks to my son Brian, who helped me keep all of this in perspective.

CS

## TABLE OF CONTENTS

| <u>Chapter</u>  | <u>Page</u> |
|---|-------------|
| ABSTRACT . . . . .  | iii         |
| ACKNOWLEDGMENTS . . . . .   | v           |
| TABLE OF CONTENTS . . . . .   | vii         |
| List of Figures . . . . .   | ix          |
| List of Tables . . . . .  | xi          |
| List of Symbols . . . . .   | xiii        |
| I. <u>INTRODUCTION</u> . . . . .  | 1           |
| A. BACKGROUND . . . . .   | 1           |
| B. BACKGROUND ON PREVIOUS RESEARCH . . . . .                            | 3           |
| C. STATEMENT OF THE PROBLEM . . . . .                                   | 5           |
| D. SUMMARY OF PRESENT WORK . . . . .                                    | 5           |
| E. THESIS OUTLINE . . . . .   | 6           |
| II. <u>CRYOGENIC HE<sup>3</sup> NUCLEAR GYRO FUNDAMENTALS</u> . . . . . | 7           |
| A. BASIC PRINCIPLES . . . . .   | 7           |
| B. PROPERTIES OF HE <sup>3</sup> . . . . .                              | 9           |
| C. MAGNETIC FIELD REQUIREMENTS . . . . .                                | 12          |
| D. MAGNETOMETER . . . . .   | 13          |
| III. <u>CROSS AXIS RATE INPUT EFFECTS</u> . . . . .                     | 15          |
| A. SENSITIVITY TO CROSS AXIS RATE INPUT . . . . .                       | 15          |
| B. RESOLUTION WITH THREE ORTHOGONAL GYROS . . . . .                     | 19          |
| C. SIGNAL LOSS DUE TO CROSS AXIS INPUTS . . . . .                       | 25          |
| D. USE OF ADDITIONAL MAGNETIC FIELDS TO NULL . . . . .                  |             |
| E. THE THREE DEGREE-OF-FREEDOM GYRO . . . . .                           | 30          |
| F. THREE ORTHOGONAL SINGLE DOF GYROS . . . . .                          | 33          |



# TABLE OF CONTENTS (Cont)

| <u>Chapter</u> |   | <u>Page</u> |
|----------------|---|-------------|
| IV.            | <u>KINEMATIC RECTIFICATION</u> . . . . .                        | 39          |
|                | A. STATEMENT OF THE PROBLEM . . . . .                           | 39          |
|                | B. ANALYSIS OF KINEMATIC RECTIFICATION EFFECTS . . .            | 41          |
|                | C. FREQUENCY DEPENDENCE . . . . .                               | 47          |
| V.             | <u>AN EXPERIMENT TO MEASURE KINEMATIC RECTIFICATION EFFECTS</u> | 53          |
|                | A. OBJECTIVE . . . . .  | 53          |
|                | B. LABORATORY FACILITIES . . . . .                              | 53          |
|                | C. BASIC CONCEPT . . . . .                                      | 56          |
|                | D. FIELD COIL DESIGN . . . . .                                  | 57          |
|                | E. EXPERIMENTAL PROCEDURE . . . . .                             | 63          |
| VI.            | <u>FIELD GRADIENT EFFECTS</u> . . . . .                         | 65          |
|                | A. FIELD GRADIENT SOURCES . . . . .                             | 65          |
|                | B. REDUCTION OF TRANSVERSE RELAXATION TIME . . . . .            | 65          |
|                | C. GRADIENT INDUCED $g$ -SENSITIVE DRIFT . . . . .              | 68          |
|                | D. GRADIENT INDUCED TEMPERATURE SENSITIVE DRIFT . . .           | 72          |
| VII.           | <u>CONCLUSIONS AND RECOMMENDATIONS</u> . . . . .                | 75          |
|                | A. CONCLUSIONS . . . . .  | 75          |
|                | B. RECOMMENDATIONS . . . . .                                    | 76          |
|                | REFERENCES . . . . .  | 77          |

# LIST OF FIGURES

| <u>Fig. No.</u> |  | <u>Page</u> |
|-----------------|--|-------------|
| I-1             | BASIC ELEMENTS OF A RING LASER GYRO . . . . .  | 2           |
| II-1            | PRECESSION OF A FREELY SPINNING BODY, POSSESSING A MAGNETIC<br>DIPOLE MOMENT $\vec{\mu}$ , IN AN APPLIED MAGNETIC FIELD, $\vec{B}$ . . . . | 8           |
| III-1           | VECTOR DESCRIPTION FOR A GENERAL CROSS AXIS RATE INPUT . .   | 16          |
| III-2           | DRIFT RATE VS LARMOR FREQUENCY FOR A NUMBER OF CROSS AXIS<br>INPUT RATES, $\omega_2$ . . . . .   | 18          |
| III-3           | COORDINATE FRAMES FOR RIGID BODY MOUNTING OF THREE IDENTI-<br>CAL GYROS . . . . .  | 20          |
| III-4           | INTERSECTING SPHERES SHOWING SOLUTIONS FOR $\vec{\omega} \cdot \vec{b} - I = 0$ . .  | 22          |
| III-5           | INTERSECTING CIRCLES SHOWING UNAMBIGUOUS CASE. . . . .   | 23          |
| III-6           | SIGNAL REDUCTION DUE TO CROSS AXIS RATE . . . . .  | 26          |
| III-7           | ANALOG SIMULATION FOR CROSS AXIS INPUTS . . . . .  | 27          |
| III-8           | MAGNETIZATION TRAJECTORY WITH OSCILLATORY . . . . .  | 29          |
| III-9           | DETERMINATION OF $\vec{\omega} \cdot \vec{G} - I$ FROM THREE MEASUREMENTS OF $M$ . .   | 31          |
| III-10          | REMOVAL OF CROSS AXIS EFFECT WITH 3 DOF GYRO SCHEME . .  | 32          |
| III-11          | EFFECT OF MEASUREMENT NOISE ON 3 DOF GYRO SCHEME . . . . .   | 34          |
| III-12          | RESPONSE TO A STEP IN $\vec{\omega} \cdot \vec{b} - I$ . . . . .   | 36          |
| IV-1            | INPUT AXIS CONING OF A SINGLE DOF GYRO . . . . .   | 40          |
| IV-2            | REFERENCE FRAMES FOR KINEMATIC RECTIFICATION ANALYSIS . .  | 42          |
| IV-3            | DRIFT VS CONING FREQUENCY . . . . .  | 49          |
| IV-4            | REGIONS OF INFLUENCE . . . . .   | 51          |
| V-1             | GENERAL EXPERIMENTAL CONFIGURATION . . . . .   | 54          |
| V-2             | SCHEMATIC DEPICTION OF THE BOTTOM PORTION OF THE CRYOSTAT<br>PROBE . . . . .   | 55          |
| V-3             | HELMHOLTZ COIL CONFIGURATION . . . . .   | 59          |
| V-4             | AXIAL FIELD PROFILES . . . . .   | 61          |

| <u>Fig. No.</u> |   | <u>Page</u> |
|-----------------|---|-------------|
| V-5             | COIL FORM ASSEMBLY . . . . .                      | 62          |
| V-6             | TR-20 CIRCUIT TO GENERATE $B_1$ . . . . .         | 64          |
| VI-1            | AXIAL FIELD PROFILE ACROSS SAMPLE CELL . . . . .  | 66          |
| VI-2            | GYRO DRIFT DUE TO CONSTANT ACCELERATION . . . . . | 71          |
| VI-3            | GYRO DRIFT DUE TO TEMPERATURE GRADIENT . . . . .  | 74          |

# LIST OF TABLES

| <u>Table No.</u> |   | <u>Page</u> |
|------------------|---|-------------|
| IV-1             | COMPARISON OF DRIFT PREDICTED BY ANALYSIS WITH CLASSICAL<br>KINEMATIC RECTIFICATION DRIFT . . . . .                   | 45          |
| IV-2             | COMPARISON OF DRIFT PREDICTED BY EQS. (4.17) AND (4.18) .   | 46          |
| IV-3             | DRIFT RATES FOR $\omega_z$ ABOVE RESONANCE . . . . .  | 48          |
| V-1              | COMPARISON OF CALCULATED DRIFT RATES WITH THOSE PREDICTED<br>BY CLASSICAL KINEMATIC RECTIFICATION EFFECTS ALONE . . . | 58          |
| V-2              | FIELD COIL SPECIFICATIONS . . . . .   | 60          |

# LIST OF SYMBOLS

|                 |         |   |
|-----------------|---------|---|
| $a$             |         | linear magnetic field gradient coefficient                  |
| $a$             | Ch. III | parameter vector  |
| $\hat{a}$       | Ch. III | estimate of $a$   |
| $A$             |         | data matrix   |
| $b$             |         | linear temperature gradient coefficient                     |
| $\vec{B}$       |         | magnetic flux density                                       |
| $B_{av}$        |         | average flux density seen by diffusing $\text{He}^3$ nuclei |
| $\vec{B}_{eff}$ |         | effective magnetic flux density                             |
| $B_0$           |         | magnetic flux density at center of sample cell              |
| $d$             |         | separation distance between coil pairs                      |
| $D$             |         | diffusion coefficient                                       |
| $g$             |         | earth's gravity ( $9.8 \text{ m/sec}^2$ )                   |
| $\hbar$         |         | Planck's constant $+ 2\pi$                                  |
| $H_0$           |         | scale height  |
| $I$             | Ch. V   | electric current  |
| $I$             |         | identity matrix   |
| $\vec{J}$       |         | angular momentum  |
| $k_B$           |         | Boltzmann's constant  |
| $\vec{M}$       |         | sample magnetization  |
| $M_0$           |         | equilibrium magnetization                                   |
| $M_s$           |         | SQUID output  |
| $\hat{n}$       |         | unit vector normal to precession plane                      |
| $N$             | Ch. V   | number of turns per coil                                    |
| $N$             |         | number of $\text{He}^3$ atoms                               |

|          |         |  |
|----------|---------|--|
| P        |         | pressure   |
| r        | Ch. V   | coil radius                                      |
| r        |         | sample cell radius as a fraction of scale height |
| R        |         | universal gas constant                           |
| $R_0$    |         | radius of sample cell                            |
| s        |         | Laplace transform variable                       |
| t        |         | time   |
| t        | Ch. VI  | $T_0/bR_0$                                       |
| T        | Ch. III | sample period                                    |
| T        |         | temperature                                      |
| $T_0$    |         | temperature at the center of the sample cell     |
| $T_1$    |         | longitudinal relaxation time                     |
| $T_2$    |         | transverse relaxation time                       |
| $T_{2G}$ |         | magnetic field gradient induced relaxation time  |
| y        |         | measurement vector                               |

#### Greek Symbols

|             |   |
|-------------|---|
| $\alpha$    | angle between measurements of $\vec{M}$     |
| $\beta$     | half angle of input axis coning motion      |
| $\gamma$    | gyromagnetic ratio                          |
| $\delta$    | unit impulse                                |
| $\delta B$  | shift in $B_{av}$ due to acceleration       |
| $\delta B'$ | shift in $B_{av}$ due to thermal gradient   |
| $\Delta t$  | elapsed time                                |
| $\theta$    | angle between $\vec{B}$ and $\vec{B}_{eff}$ |
| $\theta_1$  | rotation about $\hat{IG}$ axis              |
| $\theta_2$  | rotation about $\hat{2I}$ axis              |

|                            |   |
|----------------------------|---|
| $\vec{\mu}$                | magnetic dipole moment                  |
| $\mu_0$                    | permeability of free space              |
| $v$                        | measurement noise                       |
| $\rho$                     | density of $\text{He}^3$ sample         |
| $\rho_0$                   | sample density at center of sample cell |
| $\phi$                     | angle between $\vec{M}$ and $\hat{n}$   |
| $\vec{\omega}$             | angular velocity of rotation            |
| $\underline{\vec{\omega}}$ | $\vec{\omega}/\gamma \vec{B} $          |
| $\omega_z$                 | coning frequency                        |
| $\Omega$                   | precession frequency in G-frame         |
| $\underline{\Omega}$       | $\Omega/\gamma \vec{B} $                |

#### Superscripts

|                              |   |
|------------------------------|---|
| $A^T$                        | transpose of A                                  |
| $A^{-1}$                     | inverse of A                                    |
| $\overset{I}{\dot{\vec{M}}}$ | time rate of change of $\vec{M}$ in the I-frame |
| $\vec{\omega}^{b-I}$         | rotation of b-frame with respect to the I-frame |

#### Suffixes

|                            |                                     |
|----------------------------|-------------------------------------|
| $\mathcal{L}^{-1}\{F(s)\}$ | inverse Laplace transform of $F(s)$ |
| $\vec{M}(t)$               | time function of $\vec{M}$          |
| $\vec{M}(0)$               | initial value of $\vec{M}$          |
| $\vec{M}(n)$               | nth measure of $\vec{M}$            |
| $\delta(T)$                | unit impulse at $t = T$             |

#### Miscellaneous

|             |                        |
|-------------|------------------------|
| $ \vec{B} $ | magnitude of $\vec{B}$ |
|-------------|------------------------|

Abbreviations Used

|       |   |
|-------|---|
| cm    | centimeters                                 |
| deg   | degree                                      |
| DOF   | degree of freedom                           |
| G     | Gauss                                       |
| h     | hour  |
| Hz    | hertz                                       |
| J     | joule                                       |
| K     | degree Kelvin                               |
| m     | meter                                       |
| PR    | precession rate                             |
| rad   | radian                                      |
| SDOF  | single degree of freedom                    |
| sec   | second                                      |
| SQUID | Superconducting Quantum Interference Device |
| T     | tesla                                       |



## Chapter I

### INTRODUCTION

#### A. BACKGROUND

Bearing friction has long been recognized as a limiting factor on lifetime and accuracy for conventional mechanical gyroscopes. The evolution of these devices has proceeded through many improvements in ball bearings, raceways, and lubricants, then gas bearing technologies, and more recently, electrostatic and electromagnetic suspension schemes. The gas bearing, as well as the electrostatic and electromagnetic suspensions employ very small gaps between the rotating member and its support housing. Contaminants in these gaps, which may originate during assembly, from outgassing materials in the vicinity of the gap, or from fretting out of particulate matter during contact from starts, stops, or over-slewing, degrade performance and cause life problems.

Two nonconventional schemes were proposed in the early 1960's to eliminate bearing problems by eliminating the need to support a spinning mass. These were the ring laser gyro and the nuclear magnetic resonance gyro. There are no rotating parts, no gimbals and thus no bearings in either of these types. This aspect alone probably provided sufficient impetus for development; but there was also the potential for faster warm-up times, lower costs, and the ability to survive more severe shock and vibration environments than obtainable from mechanical gyros of comparable accuracy.

To date the ring laser gyro has already realized much of this potential, with the Honeywell version now operational on the Boeing 767 aircraft. The basic concept [Macek 1963] makes use of the high sensitivity of the oscillating frequency of a laser to dimensional variations of its resonant structure. The particular structure employed is that of a closed optical path (ring) in which light may travel in either direction (Fig. I-1). With no rotation of the ring, the clockwise and

counterclockwise beams travel the same path length in completing a pass through the ring. However, for rotations about an axis normal to the plane of the ring, the effective path lengths per pass are different for the two beams. This change in the effective lengths of the resonant structures leads to different resonant frequencies for the clockwise and counterclockwise beams. Then to first order this frequency difference is proportional to the component of the rotation normal to the plane of the ring.

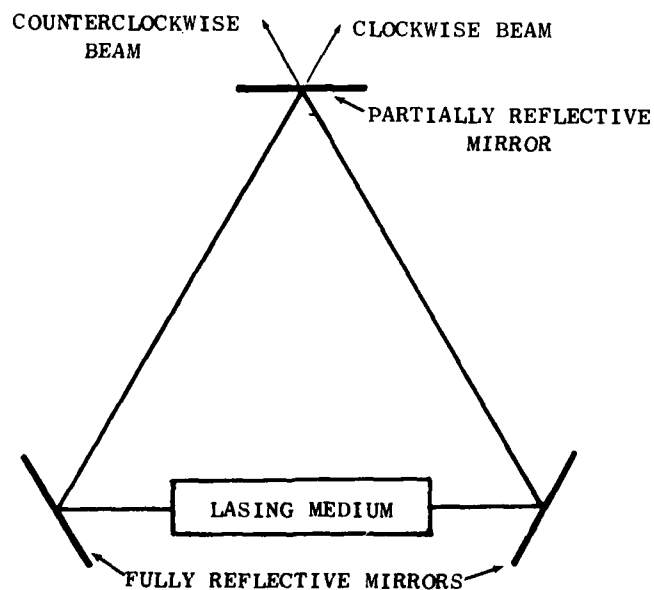


FIG. 1-1 BASIC ELEMENTS OF A RING LASER GYRO.

The basic concept of the nuclear gyro is more closely related to the mechanical gyro. Certain nuclear species possess intrinsic spin angular momentum; and this angular momentum can serve as an inertial reference in the same manner that the wheel angular momentum does for a mechanical gyro. However, since the nucleus cannot be gimballed, gimbal angles are not used to read out the spin axis direction. Instead, advantage is taken of the fact that these nuclear species possess a magnetic dipole moment which is always parallel (or always antiparallel) to the spin direction. Thus a sensitive magnetometer can be used to determine the spin direction.

The particular device under investigation here, the cryogenic  $\text{He}^3$  nuclear gyro, had yet another *raison d'être*, in addition to the previously mentioned potential advantages. Physicists have long searched for an electric dipole moment in neutrons. It was proposed [Fairbank 1967] that a nuclear gyro, using  $\text{He}^3$  as the nuclear species, with the addition of an electric field, would provide an ideal instrument for the dipole moment search (the  $\text{He}^3$  nucleus contains a single unpaired neutron). This proposal constituted the motivation for the design of a cryogenic  $\text{He}^3$  gyro to accomplish this end [Taber 1978]; and Taber's work then constituted the motivation for this thesis.

#### B. BACKGROUND ON PREVIOUS RESEARCH

The Singer Company, Kearfott Division, began work on a nuclear gyro around 1960. Their device [Simpson 1979] uses two stable, odd isotopes of mercury ( $^{199}\text{Hg}$  -  $^{201}\text{Hg}$ ) as nuclear species and a rubidium vapor optical pumping magnetometer to sense the spin axis directions of the two nuclear species. The best published results to date show a rate bias stability of  $\pm 0.312$  deg/h. The  $^{201}\text{Hg}$  species, which has a nuclear spin of  $3/2 \hbar$  and thus possesses a nuclear quadrupole moment. Electric field gradients, present at the walls of the sample cell or resulting from the light beams used for optical pumping, interact with this nuclear quadrupole moment causing the  $^{201}\text{Hg}$  spin axes to precess. This is thought to be the major perturbation to the rate bias stability in this device.

Litton Guidance & Control Systems began work on a similar device around 1968. Their device [Kanegsberg 1979] uses two noble gases ( $^{129}\text{Xe}$  -  $^{83}\text{Kr}$ ) as nuclear species and also employs a rubidium vapor optical pumping magnetometer. Like  $^{199}\text{Hg}$ ,  $^{129}\text{Xe}$  has a nuclear spin of  $1/2 \hbar$  and thus possesses no nuclear quadrupole moment.  $^{83}\text{Kr}$ , however, is a spin  $9/2 \hbar$  species thus subject to nuclear quadrupole interactions with electric field gradients. However, a more serious problem found with this device is due to a hyperfine interaction of the rubidium atoms with the noble gas atoms. The result of this interaction is the presence of an effective magnetic field at the noble gas nucleus during collision with a rubidium atom. Since the magnitude of this effective field is different for the two nuclear species, a rate bias results. This interaction was also found to cause large sensitivities to optical pumping lamp intensities and to temperature. Kanegsberg's report does not present any rate bias stability data but does indicate that the present model can be easily compensated to yield 10 deg/h.

The cryogenic  $\text{He}^3$  nuclear gyro, being developed here at Stanford University, employs only a single species,  $\text{He}^3$ . Since  $\text{He}^3$  is a spin  $1/2 \hbar$  species, it possesses no nuclear quadrupole moment. Then, since the rubidium vapor optical pumping magnetometer is not used, this device is not subject to the hyperfine interaction mentioned previously. The major difficulty with any single species device is that it makes no distinction between a shift in the ambient magnetic field and an actual rotation. Thus it is imperative to strictly control the magnetic environment. Fortunately much successful work had preceded this effort to establish very low, homogeneous, stable magnetic fields inside superconducting shields [Cabrera 1975]. Another difficulty with the  $\text{He}^3$  nuclear gyro is that, at the cryogenic operating temperatures, optical pumping is not possible. Thus long relaxation times (see Ch. II) are necessary for a practical  $\text{He}^3$  nuclear gyro. A longitudinal relaxation time of 140 hours was obtained in a pyrex sample cell under the cryogenic environment proposed for this gyro [Taber 1978]. Taber has also performed the analysis to predict the effects that dimensional variations, temperature variations, magnetometer noise, gyro housing asymmetries, and London moment will have on the bias stability of this gyro.

### C. STATEMENT OF THE PROBLEM

The purpose of this research is to analyze the expected performance of the  $\text{He}^3$  gyro with respect to vibrations, rotations, and accelerations, such as would be encountered in typical gyro applications. Previous work on the cryogenic  $\text{He}^3$  nuclear gyro involved a detailed development of the theory of relaxation, relaxation measurements under a number of situations, and an analysis of the expected performance of the  $\text{He}^3$  gyro with respect to the requirements of the  $\text{He}^3$  electric dipole moment experiment [Taber 1978]. For the purposes of that experiment, only a single gyro--with its input axis aligned with the earth's rotational velocity--was needed. Mechanical motions were deliberately kept to a minimum, i.e., to the extent that the experiment was conducted on a concrete isolation pad which was separate from the building floor.

### D. SUMMARY OF PRESENT WORK

The principal contributions of this research are listed below.

- A theoretical analysis of the effects of cross axis inputs, including a prediction that certain oscillatory rate inputs could precess the sample magnetization toward the applied magnetic field, thus reducing the signal to noise of the gyro.
- A theoretical analysis of rectification of oscillatory inputs including both rectification of oscillatory cross axis inputs and kinematic rectification.
- Modification of Taber's laboratory equipment provided a device which could be tested as a nuclear gyro.
- Design of an experiment to use the above device to verify the predicted kinematic rectification effects which produce drift in the presence of coning motion.
- A theoretical analysis of the effects of acceleration and temperature gradients in the presence of a linear gradient in the ambient magnetic field.

## E. THESIS OUTLINE

Chapter II outlines the basic principles of the cryogenic  $\text{He}^3$  nuclear gyro. The Bloch equations, which describe the dynamics of the device, are presented.

In Chapter III there is given a theoretical analysis of cross axis effects. The analysis predicts the presence of a false solution when three rigidly mounted orthogonal nuclear gyros are used to determine the rotational rate of a body to which the gyro triad is attached. Also predicted is that certain oscillatory rates can cause the sample magnetization to align with the applied magnetic field. This is important because this condition of alignment results in no output signal. An algorithm is developed to resolve the ambiguity without the need for an additional gyro; and it is shown that this algorithm may be used in conjunction with additional magnetic field coils to keep the sample magnetization orthogonal to the applied field.

The phenomenon of kinematic rectification is analyzed in Chapter IV. It is shown that, as the coning frequency increases, the drift approaches a maximum value that depends only on the coning angle. This is different from the classical concept of kinematic rectification.

Chapter V describes an experiment to verify the predicted kinematic rectification effects. The salient features of the experiment are that it may be conducted with a relatively simple apparatus; and, by using rotating magnetic fields, no mechanical coning motions are required.

In Chapter VI some effects of magnetic field gradients are investigated. Previous work [Taber 1978] had shown the importance of magnetic field stability and that relaxation times are reduced by the presence of a magnetic field gradient. This analysis shows that a linear gradient in the magnetic field also introduces a sensitivity to acceleration and temperature gradients. These sensitivities are theoretically predicted as functions of sample cell size, temperature, acceleration, and the magnitudes of the temperature and magnetic field gradients.

Chapter II  
CRYOGENIC  $\text{He}^3$  NUCLEAR GYRO FUNDAMENTALS

A. BASIC PRINCIPLES\*

Consider a freely spinning body which possesses a magnetic dipole moment,  $\vec{\mu}$ . Furthermore, consider that  $\vec{\mu}$  is colinear with the angular momentum  $\vec{j}$  of the body such that

$$\vec{\mu} = \gamma \vec{j} \quad (2.1)$$

where  $\gamma$  is a constant. Now place this body in a uniform magnetic field  $\vec{B}$ . This will produce a torque of  $\vec{\mu} \times \vec{B}$  on the body; and the classical equation of motion of  $\vec{j}$  is

$$\frac{d\vec{j}}{dt} = \vec{\mu} \times \vec{B} \quad (2.2)$$

Or making use of the relation between  $\vec{j}$  and  $\vec{\mu}$

$$\frac{d\vec{\mu}}{dt} = \vec{\mu} \times \gamma \vec{B} \quad (2.3)$$

One might consider basing a gyro design on such a body in the following way. Place the freely spinning body in a gyro housing and apply a uniform magnetic field that is fixed in the gyro housing coordinates. Then if the gyro or G-coordinate frame is defined such that  $\vec{B} = B_3 \hat{G}$ , we can write (2.3) in the G-frame as

---

\* Classical treatments of the equation of motion of  $\vec{\mu}$  in a magnetic field can be found in Kittel [1976] or Cohen-Tannoudji [1977]. The same results are derived via a quantum mechanical treatment [Abraham 1973].

$$\frac{d\vec{\mu}}{dt} = \frac{\vec{I}}{\mu} - \frac{\vec{G}-\vec{I}}{\omega} \times \vec{\mu} . \quad (2.4)$$

If we consider the case where the gyro frame is nonrotating with respect to an inertial frame, that is  $\frac{d\vec{G}-\vec{I}}{\omega} = 0$ , then expanding (2.4) into rectangular components in the G-frame, we get

$$\frac{d}{dt} \begin{bmatrix} \mu_1 \\ \mu_2 \\ \mu_3 \end{bmatrix} = \begin{bmatrix} 0 & \gamma B_3 & 0 \\ -\gamma B_3 & 0 & 0 \\ 0 & 0 & 0 \end{bmatrix} \begin{bmatrix} \mu_1 \\ \mu_2 \\ \mu_3 \end{bmatrix} . \quad (2.5)$$

We see that  $\mu_3$  is uncoupled from  $\mu_1$  and  $\mu_2$ , and is constant. The solution for  $\mu_1$  and  $\mu_2$  is that of a sinusoidal oscillator with frequency  $\gamma B_3$  rad/sec. A general solution for  $\vec{\mu}$  is shown in Fig. II-1. The angle,  $\theta$ , between  $\vec{\mu}$  and  $\vec{B}$  remains constant while  $\vec{\mu}$  precesses around  $\vec{B}$  at a radian frequency of  $\gamma B_3$ .

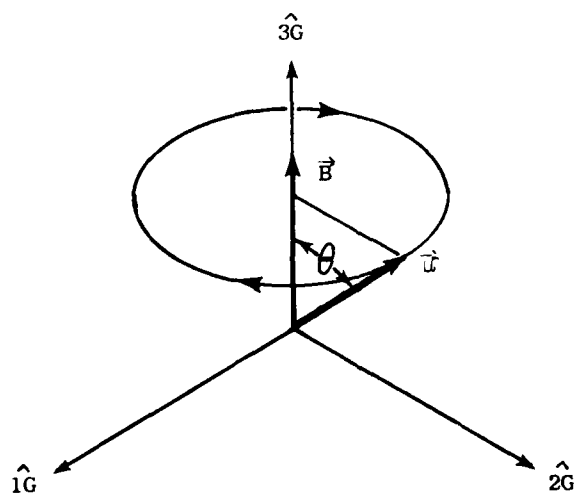


FIG. II-1 PRECESSION OF A FREELY SPINNING BODY, POSSESSING A MAGNETIC DIPOLE MOMENT  $\vec{\mu}$ , IN AN APPLIED MAGNETIC FIELD,  $\vec{B}$ . The direction of precession is that for a positive gyromagnetic ratio  $\gamma$ .



Now for the case where  $\vec{\omega}^{G-I} = \vec{\omega}_3 \hat{3G}$  we get, in the G-frame

$$\frac{d}{dt} \begin{bmatrix} \mu_1 \\ \mu_2 \\ \mu_3 \end{bmatrix} = \begin{bmatrix} 0 & (\gamma B_3 + \omega_3) & 0 \\ -(\gamma B_3 + \omega_3) & 0 & 0 \\ 0 & 0 & 0 \end{bmatrix} \begin{bmatrix} \mu_1 \\ \mu_2 \\ \mu_3 \end{bmatrix} \quad (2.6)$$

The form of the solution is the same as (2.5), but the precession frequency is now  $(\gamma B_3 + \omega_3)$  rad/sec. Thus if we know  $\gamma B_3$  and observe either component  $\mu_1$  or  $\mu_2$  with a magnetometer, fixed to the gyro housing, we can measure  $(\gamma B_3 + \omega_3)$  to determine  $\omega_3$ . Alternatively, we could compare the phase of  $\mu_1$ , (or  $\mu_2$ ), to that of a stable oscillator with radian frequency  $\gamma B_3$  and initially at the same phase as  $\mu_1$  (or  $\mu_2$ ). A phase difference would then be a measure of the angular displacement of the G-frame with respect to the I-frame about the  $\hat{3G}$  axis. The question of how to handle components of  $\vec{\omega}^{G-I}$  orthogonal to the  $\hat{3G}$  axis is addressed in Ch. III. It is seen that as long as these components are small compared to  $\gamma B_3$ , then Eq. (2.6) is correct to first order. Thus if we can come up with a suitable freely spinning body, a gyro housing, a magnetometer, and a uniform magnetic field, we have the potential for constructing a single degree-of-freedom gyro that can be used in either a rate or rate-integrating mode.

### B. PROPERTIES OF $\text{He}^3$

One such body that possesses the requisite characteristics is the nucleus of the  $\text{He}^3$  atom. It has intrinsic spin angular momentum of  $1/2 \hbar$ , a gyromagnetic ratio  $\gamma$ , of  $-2.038 \times 10^4 \text{ rad-sec}^{-1} \text{-G}^{-1}$  ( $-3.244 \times 10^7 \text{ Hz-T}^{-1}$ ), and a magnetic dipole moment of  $1.075 \times 10^{-23} \text{ erg-G}^{-1}$  ( $1.075 \times 10^{-26} \text{ J-T}^{-1}$ ). Thus we cannot consider using only a single atom but rather a collection of a large number of  $\text{He}^3$  atoms. The magnetometer then senses the net effect of the individual dipole moments, the magnetization of the collective sample, which is defined as

$$\vec{M} = \frac{1}{\text{vol}} \sum_{i=1}^N \vec{\mu}_i \quad (2.7)$$

where  $N$  = number of  $\text{He}^3$  atoms.

How then will this collection of atoms behave? The individual nuclei cannot truly be considered freely rotating bodies since they will influence each other via dipole - dipole interactions and will suffer collisions with the walls of the containment vessel. Let us first look at the equilibrium condition of this collection in a uniform magnetic field. Since the energy of a dipole in an external field is  $-\vec{\mu} \cdot \vec{B}$ , then it is energetically favorable for the dipoles to align with the applied field. Thus we would expect to find a component of  $\vec{M}$  along  $\vec{B}$  at equilibrium. There is no such energy distinction for components of  $\vec{M}$  orthogonal to  $\vec{B}$  and thus at equilibrium we would expect to have random distribution of these components leading to a zero magnetization in that plane. Boltzmann statistics give the equilibrium value of the magnetization, at temperature  $T$ , to be

$$M_0 = N|\vec{\mu}| \tanh \left( \frac{|\vec{\mu}||\vec{B}|}{k_B T} \right). \quad (2.8)$$

Referring to (2.4) and remembering that we are interested in measuring the component of  $\vec{\omega}^{G-I}$  along the  $\hat{3G}$  axis, we see that the equilibrium condition is of no use since  $\vec{\mu} \approx 0$  here. So we must consider conditions perturbed from equilibrium. In particular, suppose we prepare the  $\text{He}^3$  sample to have a nonzero magnetization in the  $\hat{1G}$  direction. One means of accomplishing this is via a process called optical pumping [Colegrove 1963]. If we now apply a field along the  $\hat{3G}$  axis, then those dipoles not aligned with the field  $\vec{B}$  will precess about  $\vec{B}$  at the radian frequency  $\gamma B$ . This is referred to as 'Larmor precession' and  $\gamma B$  is the Larmor frequency. For  $\vec{B}$  uniform, the Larmor frequency is the same for each of the precessing dipoles; and thus, if we start out with a nonzero magnetization, it too, will precess at the Larmor frequency.

In addition to the Larmor precession, the  $\text{He}^3$  sample will relax back to its equilibrium state. If we assume that the equilibrium state is approached at a rate proportional to the displacement from equilibrium, then the relaxation of  $M_3$  is described by the differential equation

$$\frac{d}{dt} M_3 = \frac{M_0 - M_3}{T_1} . \quad (2.9)$$

The characteristic time  $T_1$  is referred to as the longitudinal relaxation time. Similarly for  $M_1$  and  $M_2$ , which have zero equilibrium values, we get

$$\frac{d}{dt} M_1 = - \frac{M_1}{T_2} \quad (2.10)$$

$$\frac{d}{dt} M_2 = - \frac{M_2}{T_2} . \quad (2.11)$$

The characteristic time  $T_2$  is referred to as the transverse relaxation time.  $T_1$  and  $T_2$  may be nearly equal; but, in general,  $T_1$  is greater than  $T_2$  for reasons that will become apparent later.

Now combining both the Larmor precession and relaxation effects, we get the Bloch equations [Kittel 1976] in the gyro frame:

$$\frac{d}{dt} M_1 = \gamma(\vec{M} \times \vec{B})_1 - (\vec{\omega}^{G-I} \times \vec{M})_1 - \frac{M_1}{T_2} \quad (2.12)$$

$$\frac{d}{dt} M_2 = \gamma(\vec{M} \times \vec{B})_2 - (\vec{\omega}^{G-I} \times \vec{M})_2 - \frac{M_2}{T_2} \quad (2.13)$$

$$\frac{d}{dt} M_3 = \gamma(\vec{M} \times \vec{B})_3 - (\vec{\omega}^{G-I} \times \vec{M})_3 + \frac{M_0 - M_3}{T_1} . \quad (2.14)$$

For a liquid sample of  $\text{He}^3$  in  $\text{He}^4$ , with a solid hydrogen wall coating, a  $T_2$  of 140 hours has been obtained. Thus for many calculations, particularly those involving short term effects, the relaxation terms may be neglected. The gyro modeling performed in the following chapters will generally employ this assumption.

### C. MAGNETIC FIELD REQUIREMENTS

One obvious difficulty in making a practical  $\text{He}^3$  nuclear gyro is in obtaining a uniform, static magnetic field. The magnitude of the earth's magnetic field is on the order of 0.5G ( $5 \times 10^{-5}\text{T}$ ) at the surface and varies in magnitude and direction from one location to another. So one task is to screen the  $\text{He}^3$  sample from the ambient magnetic field. Cabrera [Cabrera 1975] has developed a method of creating low field,  $10^{-8}\text{G}$  ( $10^{-12}\text{T}$ ), regions within a superconducting lead foil shield. This type of shield has the property of perfect diamagnetism. That is, beyond a penetration depth which is much smaller than the foil thickness, the magnetic flux density in the foil is zero. This is only true provided the ambient field remains below a critical value and the temperature remains below a critical value. For lead, the critical magnetic field is 803 G ( $8.03 \times 10^{-2}\text{T}$ ) and the critical temperature is 7.2K. It is not difficult to avoid encountering a critical field, but to maintain the lead foil below 7.2K requires that the shield be kept in a liquid helium bath.

In addition to shielding from outside magnetic fields, it is also required that a high degree of uniformity of the applied field,  $\vec{B}$ , be achieved. If sixth order Helmholtz coils are used to generate  $\vec{B}$ , then gradients in  $\vec{B}$  will be due mainly to the inhomogeneities in the trapped field. Based on current capabilities the major field inhomogeneity is estimated to be a linear gradient of magnitude less than  $10^{-8}\text{G}\cdot\text{cm}^{-1}$  ( $10^{-10}\text{T}\cdot\text{m}^{-1}$ ) [Taber 1978].

Furthermore the field coils could be made with superconducting wire so that the field will be generated by the persistent supercurrent, which is inherently very stable.

#### D. MAGNETOMETER

The remaining element of the  $\text{He}^3$  nuclear gyro is the sensor, the magnetometer. Since there is already a requirement to maintain the shield and the field coils at cryogenic temperatures, a natural candidate for a magnetometer is the SQUID (Superconducting Quantum Interference Device) magnetometer. Fortunately, this is the most sensitive magnetometer currently available. Theory and use of the SQUID are described in such references as Giffard [1972], Zimmerman [1970], and Silver [1967]\*; SQUID use for a  $\text{He}^3$  nuclear gyro is described by Taber [Taber 1978].

---

\* See also the S.H.E. Corp. Catalog

### Chapter III

#### CROSS AXIS RATE INPUT EFFECTS

##### A. SENSITIVITY TO CROSS AXIS RATE INPUT

Having a basis for using a  $\text{He}^3$  nuclear gyro for measuring rotations about the applied field axis, consider now the effects of rotations about orthogonal axes. Suppose, as shown in Fig. III-1, that  $B = B_3 \hat{z}$  and  $\vec{\omega} = \omega_2 \hat{y}$ . Then appealing to (2.12), (2.13), and (2.14), and neglecting the relaxation terms, we get

$$\frac{G}{M} = \frac{I}{M} + \vec{\omega} \times \vec{M}. \quad (3.1)$$

Thus

$$\frac{G}{M} = \begin{bmatrix} 0 & \gamma B_3 & -\omega_2 \\ -\gamma B_3 & 0 & 0 \\ \omega_2 & 0 & 0 \end{bmatrix} \vec{M}. \quad (3.2)$$

Solving via Laplace transforms, in the gyro frame

$$\vec{M}(t) = f^{-1} \left\{ \left( sI - \begin{bmatrix} 0 & \gamma B_3 & -\omega_2 \\ -\gamma B_3 & 0 & 0 \\ \omega_2 & 0 & 0 \end{bmatrix} \right)^{-1} \right\} \vec{M}(0) \quad (3.3)$$

$$= \begin{bmatrix} \cos \omega t & \frac{\gamma B_3}{\omega} \sin \omega t & -\frac{\omega_2}{\omega} \sin \omega t \\ -\frac{\gamma B_3}{\omega} \sin \omega t & \cos \omega t + \left(\frac{\omega_2}{\omega}\right)^2 (1 - \cos \omega t) & \frac{\gamma B_3 \omega_2}{\omega^2} (1 - \cos \omega t) \\ \frac{\omega_2}{\omega} \sin \omega t & \frac{\gamma B_3 \omega_2}{\omega^2} (1 - \cos \omega t) & \cos \omega t + \left(\frac{\gamma B_3}{\omega}\right)^2 (1 - \cos \omega t) \end{bmatrix} \vec{M}(0) \quad (3.4)$$

$$\text{where} \quad \omega^2 = (\gamma B_3)^2 + \omega_2^2. \quad (3.5)$$

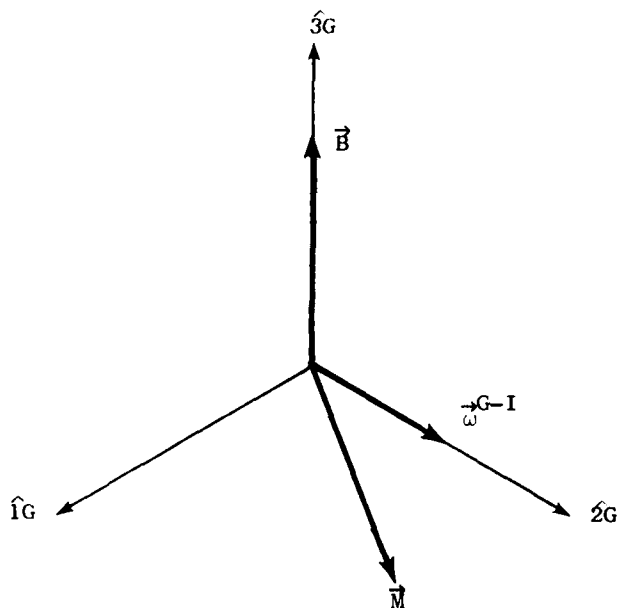


FIG. III-1 VECTOR DESCRIPTION FOR A GENERAL CROSS AXIS RATE INPUT.

One effect of a cross axis input is immediately apparent. Even with no component of rotation about the applied field (input) axis, the precession frequency, seen in the G-frame, is  $[(\gamma B_3)^2 + \omega_2^2]^{\frac{1}{2}}$  rad/sec. If uncorrected, the reading from this gyro will be in error by  $(\omega - \gamma B_3)$  rad/sec.

$$(\omega - \gamma B_3) = [(\gamma B_3)^2 + \omega_2^2] \quad (3.6)$$

$$(\omega - \gamma B_3) = \gamma B_3 \left\{ \left[ 1 + \left( \frac{\omega_2}{\gamma B_3} \right)^2 \right]^{\frac{1}{2}} - 1 \right\}. \quad (3.7)$$

Then expanding the term in brackets in (3.7) and keeping only the first term in  $(\omega_2/\gamma B_3)^2$  shows that the drift due to a cross axis input rate,  $\omega_2$ , is on the order of  $\frac{1}{2}(\omega_2^2/\gamma B_3)$  rad/sec.

Figure III-2 shows the effect of an uncorrected cross axis input. As shown above the drift grows as  $\omega_2^2$  and inversely with the Larmor frequency,  $\gamma B_3$ . This suggests that cross coupling effects can be made arbitrarily small simply by increasing  $B_3$ . However, for a cross axis input rate of 1.0 rad/sec, the Larmor frequency must be  $10^7$  rad/sec to reduce the uncorrected drift to  $5 \times 10^{-8}$  rad/sec (0.01 deg/h). For  $\text{He}^3$  this requires that  $B_3$  be about 490 G ( $4.9 \times 10^{-2}$  T). The gradients associated with such large fields make them impractical. The better approach is to measure the cross axis inputs and then compensate for their effects.

So let us consider the general case where there is both an input axis and a cross axis component of the input rate. Take the two respective components of  $\vec{\omega}^{G-I}$  to be  $\omega_3 \hat{3G}$  and  $\omega_2 \hat{2G}$ . There is no loss of generality here since the direction of the  $\hat{2G}$  axis, in the plane normal to the  $\hat{3G}$  axis, is arbitrary. Proceeding as before, we get

$$\frac{G}{\vec{M}} = \begin{bmatrix} 0 & (\gamma B_3 + \omega_3) & -\omega_2 \\ -(\gamma B_3 + \omega_3) & 0 & 0 \\ \omega_2 & 0 & 0 \end{bmatrix} \vec{M}. \quad (3.8)$$

The solution is thus the same as (3.4) with the term  $\gamma B_3$  replaced by  $(\gamma B_3 + \omega_3)$ . Thus the precession frequency seen in the G-frame is now  $\gamma[(B_3 + \omega_3/\gamma)^2 + (\omega_2/\gamma)^2]^{1/2}$ . It can also be shown that the normal to the tip path plane (precession plane) of  $\vec{M}$  is parallel to  $\gamma(B_3 + \omega_3/\gamma) \hat{3G} + \gamma(\omega_2/\gamma) \hat{2G}$ . That is the behavior which is identical to the case where  $\vec{\omega}^{G-I} = 0$  and the applied field is

$$\vec{B} = (B_3 + \frac{\omega_3}{\gamma}) \hat{3G} + (\frac{\omega_2}{\gamma}) \hat{2G}.$$

This is simply a statement of the equivalence between rotations and magnetic fields [Abragam 1973]. Thus the effect of a cross axis rotation,  $\omega_2$ , is the same as that of applying a magnetic field,  $\omega_2/\gamma$ , in the same



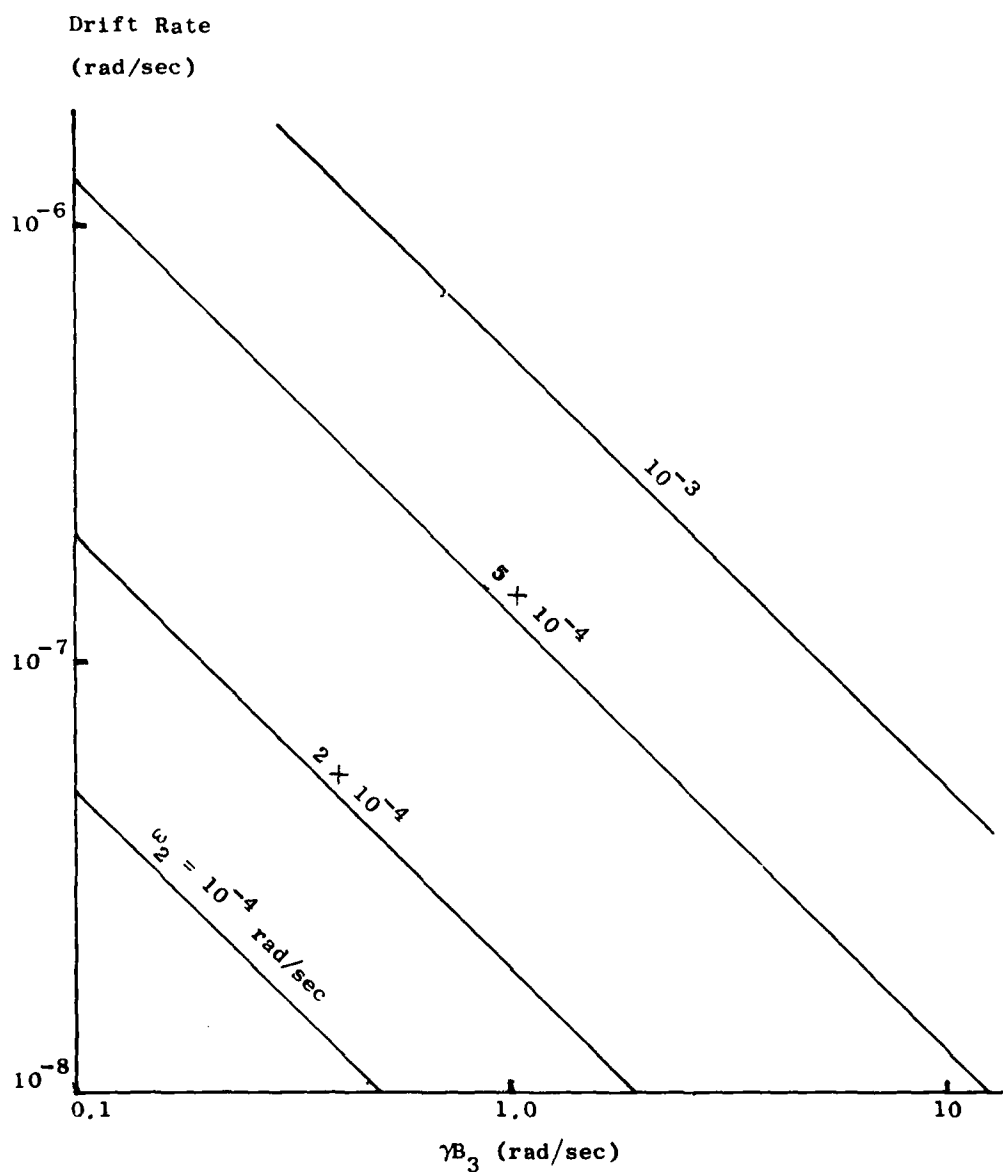


FIG. III-2 DRIFT RATE VS LARMOR FREQUENCY FOR A NUMBER OF CROSS  
AXIS INPUT RATES,  $\omega_2$ .

direction as the cross axis component of  $\vec{\omega}^{G-I}$ . Thus, if  $\vec{\omega}^{G-I} = \omega_1 \hat{1}G + \omega_2 \hat{2}G + \omega_3 \hat{3}G$ , the sensed precession frequency,  $\Omega$ , will be given by

$$\Omega = [(\gamma B_3 + \omega_3)^2 + \omega_2^2 + \omega_1^2]^{\frac{1}{2}} \quad (3.9)$$

#### B. RESOLUTION WITH THREE ORTHOGONAL GYROS

As we saw in general, the uncorrected drift,  $[\Omega - (\gamma B_3 + \omega_3)]$  is not tolerable. So consider using three identical gyros, rigidly aligned, such that their input axes are orthogonal (Fig. III-3). Then each gyro will undergo the same rotation but, because the input axes are orthogonal, each will be affected differently.

For the case where  $\vec{\omega}^{b-I} = \omega_1 \hat{1}b + \omega_2 \hat{2}b + \omega_3 \hat{3}b$ , the precession frequencies sensed by each gyro are

$$\Omega_1^2 = (\gamma B_3 + \omega_1)^2 + \omega_2^2 + \omega_3^2 \quad (3.10a)$$

$$\Omega_2^2 = \omega_1^2 + (\gamma B_3 + \omega_2)^2 + \omega_3^2 \quad (3.10b)$$

$$\Omega_3^2 = \omega_1^2 + \omega_2^2 + (\gamma B_3 + \omega_3)^2 \quad (3.10c)$$

It is convenient to normalize by dividing both sides of the above by  $(\gamma B_3)^2$ , giving:

$$\frac{\Omega_1^2}{(\gamma B_3)^2} = (1 + \frac{\omega_1}{\gamma B_3})^2 + \frac{\omega_2^2}{(\gamma B_3)^2} + \frac{\omega_3^2}{(\gamma B_3)^2} \quad (3.11a)$$

$$\frac{\Omega_2^2}{(\gamma B_3)^2} = \frac{\omega_1^2}{(\gamma B_3)^2} + (1 + \frac{\omega_2}{\gamma B_3})^2 + \frac{\omega_3^2}{(\gamma B_3)^2} \quad (3.11b)$$

$$\frac{\Omega_3^2}{(\gamma B_3)^2} = \frac{\omega_1^2}{(\gamma B_3)^2} + \frac{\omega_2^2}{(\gamma B_3)^2} + (1 + \frac{\omega_3}{\gamma B_3})^2 \quad (3.11c)$$

where the underbars indicate normalized quantities.

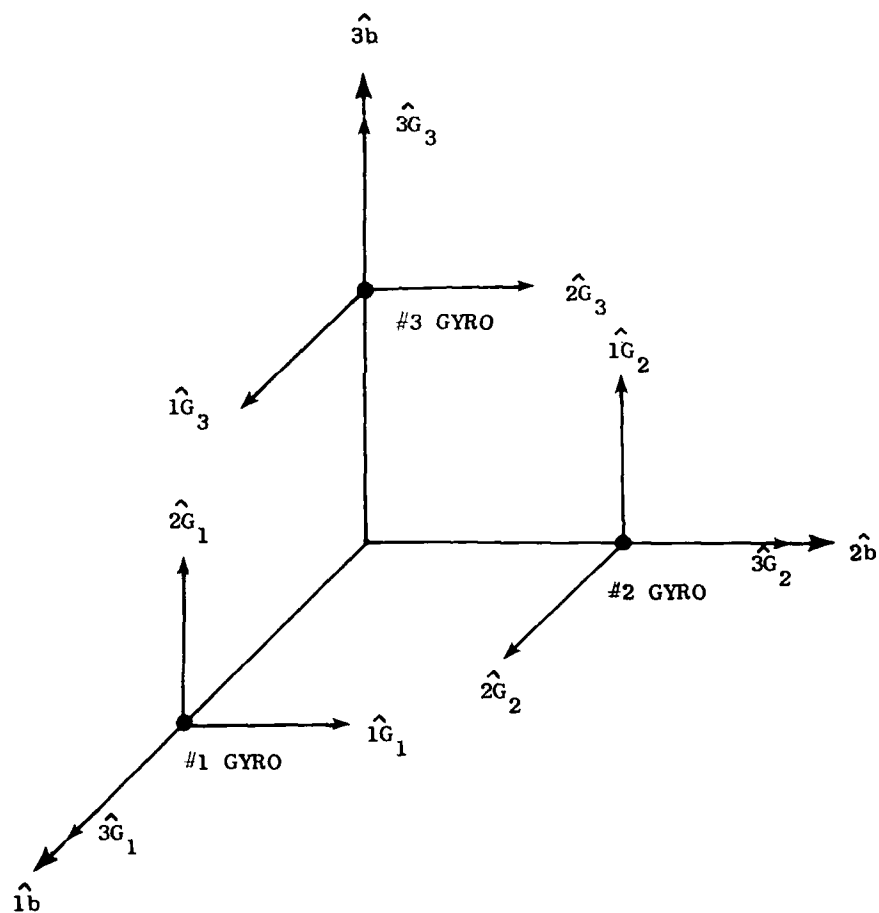


FIG. III-3 COORDINATE FRAMES FOR RIGID BODY MOUNTING OF THREE IDENTICAL GYROS. The b-frame is the body frame.

Now the question is, do Eqs. (3.11) uniquely determine  $\vec{\omega}^{b-I}$ , and, in general, the answer is no. Knowledge of the time history of  $\vec{\omega}^{b-I}$  will not resolve the ambiguity, as the following example will show. Suppose initially  $\vec{\omega}^{b-I} = -1/3 \hat{1}b - 1/3 \hat{2}b - 1/3 \hat{3}b$ . This particular case is resolved unambiguously from (3.11). Furthermore, assume that this condition persists for some time. Then suppose the input changes such that  $\vec{\omega}^{b-I} = -0.3333 \hat{1}b - 0.3333 \hat{2}b - 0.3333 \hat{3}b$ . With only the measurements  $\Omega_1, \Omega_2, \Omega_3$  and knowledge of  $\gamma B_3$ , two solutions for  $\vec{\omega}^{b-I}$  are possible. One solution is indeed the true solution; the other, however, is  $\vec{\omega}^{b-I} = -0.33337 \hat{1}b - 0.33337 \hat{2}b - 0.33337 \hat{3}b$ . The two solutions are nearly equal, though in opposite directions from the previous known solution. The smaller the step away from  $-1/3 \hat{1}b - 1/3 \hat{2}b - 1/3 \hat{3}b$  the closer are the two solutions. Thus it is easy to conceive of the possibility of locking on to the false solution from this starting point.

Let us investigate the source of the ambiguity by considering the space of possible inputs,  $\vec{\omega}^{b-I}$ ,  $(\omega_1, \omega_2, \omega_3)$ , in which we graph (3-11). Figure III-4 shows the case where  $\vec{\omega}^{b-I} = 0$ . Here the false solution is  $(-2/3, -2/3, -2/3)$ , and  $\Omega_1 = \Omega_2 = \Omega_3 = 1.0$ . We see that the information from any one gyro defines a sphere on which the possible values of  $\vec{\omega}^{b-I}$  lie. The solution(s) then will be the point(s) common to all three spheres. Figure III-4 is an isometric drawing and so the two solutions plot as the same point; nevertheless one can easily visualize the false solution for this case. Note that for three identical gyros that the centers for the three spheres are located at  $(-1, 0, 0)$ ,  $(0, -1, 0)$ , and  $(0, 0, -1)$  and the corresponding radii are  $\Omega_1, \Omega_2$ , and  $\Omega_3$ .

To explore this situation further, consider the condition that  $\vec{\omega}^{b-I}$  lies in the plane defined by the centers of the three spheres. As can be seen from Fig. III-5, there can be no false solution. In this plane the solution is the intersection of three circles. Then, since the three centers are not colinear, there will be at most one point of intersection. And since as one moves out of this plane in either direction, the surfaces of the three spheres will be moving away from

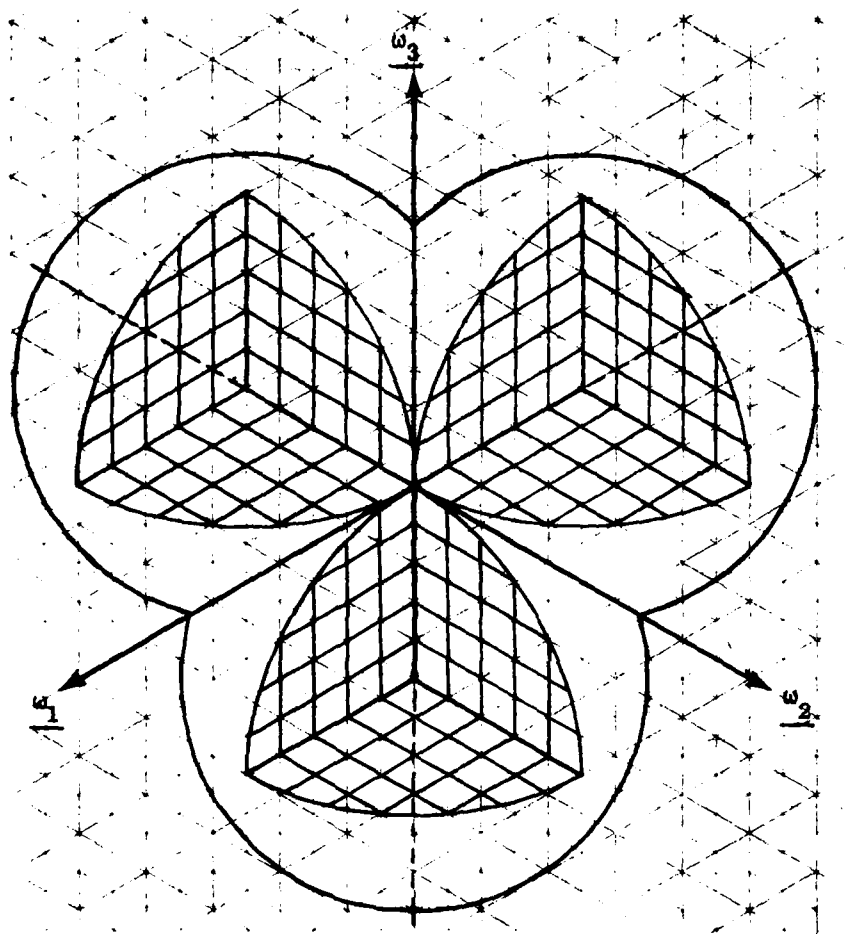


FIG. III-4 INTERSECTING SPHERES SHOWING SOLUTIONS FOR  $\vec{b} - I = 0$ . Note the two solutions are  $(0, 0, 0)$  and  $(-\frac{2}{3}, -\frac{2}{3}, -\frac{2}{3})$ .

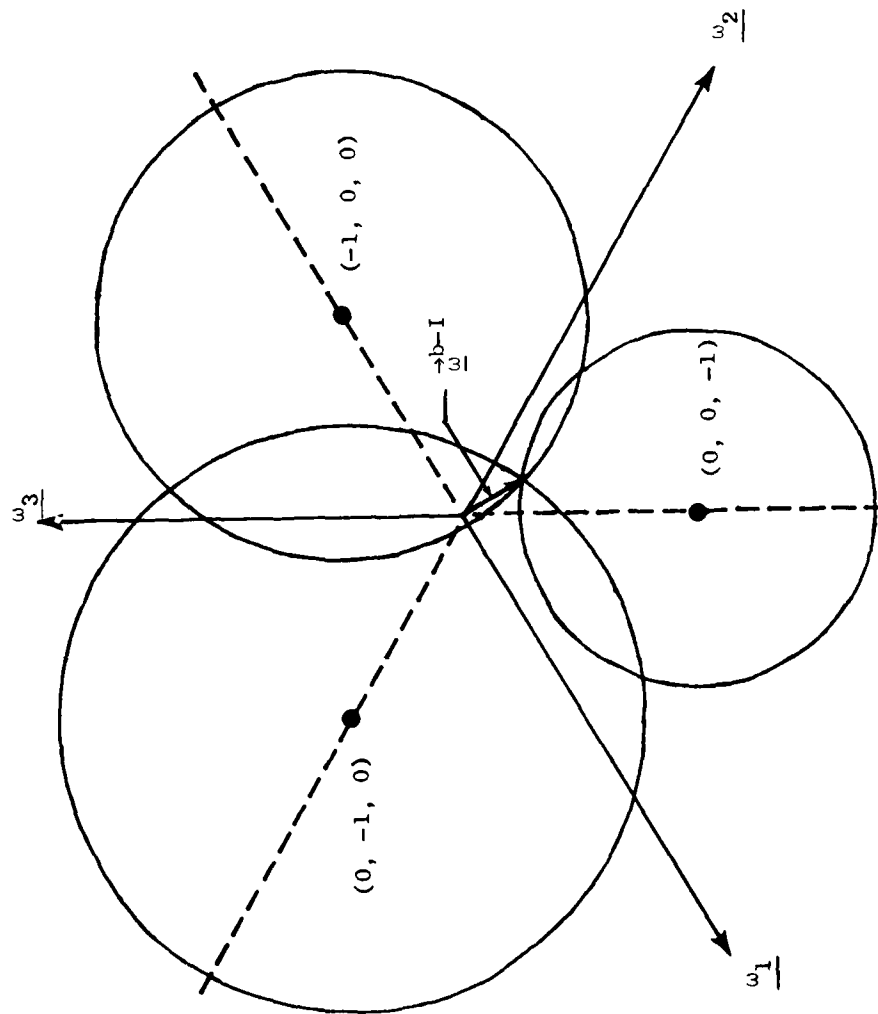


FIG. III-5 INTERSECTING CIRCLES SHOWING UNAMBIGUOUS CASE.  $\vec{u}^{b-I} = -\frac{2}{6} \vec{u}^b - \frac{1}{6} \vec{u}^2 - \frac{3}{6} \vec{u}^3$  is in the plane of centers.

one another, there can be no further points of intersection. So the plane of centers defined by (3.12) is the only region where

$$\sum_{i=1}^3 \underline{\omega}_i = -1 \quad (3.12)$$

the solution is unambiguous.

What then is the nature of the ambiguity? Consider the case where  $\underline{\omega}^{b-I}$  lies outside the plane of centers. Choosing any two of the spheres we see that their intersection must be a circle. Furthermore, the plane of centers cuts this circle in half; i.e., the center of this circle lies in the plane of centers. Now since the third sphere must also pass through  $\underline{\omega}^{b-I}$ , this sphere will intersect the circle at two points. One is indeed at  $\underline{\omega}^{b-I}$  and the second point is the reflection of  $\underline{\omega}^{b-I}$  across the plane of centers.

We can now propose a simple criterion for resolving ambiguities. Since one would want to stay away from the resonance condition ( $\underline{\omega}^{b-I} = \gamma B_3$ ) in general, the Larmor frequency could be chosen such that

$$\sum_{i=1}^3 \underline{\omega}_i^{b-I} \geq -\gamma B_3$$

for all allowable  $\underline{\omega}^{b-I}$ . Then the proper choice of solutions will always be on the same side of the plane of centers. Another possible criterion, though more restrictive, would be to choose

$$|\gamma B_3| \geq \sqrt{3} |\underline{\omega}^{b-I}|_{\max};$$

then the proper solution will be the one with the magnitude less than  $1/\sqrt{3} (|\gamma B_3|)$ .

### C. SIGNAL LOSS DUE TO CROSS AXIS INPUTS

The other effect of a cross axis rotation is to tilt the precession plane such that it is normal to the effective field,  $\vec{B}_{\text{eff}}$

$$\vec{B}_{\text{eff}} = \frac{\omega_1}{\gamma} \hat{I}G + \frac{\omega_2}{\gamma} \hat{2}G + (B_3 + \frac{\omega_3}{\gamma}) \hat{3}G. \quad (3.13)$$

The instantaneous normal to the precession plane will always be in the direction of  $\vec{B}_{\text{eff}}$ ; however, the manner in which the normal tracks  $\vec{B}_{\text{eff}}$  depends on how fast  $\vec{B}_{\text{eff}}$  changes direction and on the initial conditions of  $\vec{M}$  when the change transpires. If  $\vec{M}$  initially lies in the plane of precession, this condition can be maintained provided the rate of change of direction of  $\vec{B}_{\text{eff}}$  is small compared to  $|\gamma B_{\text{eff}}|$ .

Violation of this condition will result in  $\vec{M}$  tracing out a cone around  $\vec{B}_{\text{eff}}$ . As an example, consider the extreme case where initially  $\vec{B}_{\text{eff}} = B_3 \hat{3}G$ ; then as  $\vec{M}$  points along the  $\hat{2}G$  axis, there is an instantaneous change in  $\frac{\omega_2}{\gamma} \hat{2}G$  to be  $-\omega_2 \hat{2}G$ . This tilts the effective field toward the  $\hat{2}G$  direction. Now  $\vec{M}$  maintains a fixed angle with respect to  $\vec{B}_{\text{eff}}$  and thus moves up out of the horizontal plane (see Fig. III-6). If at some time later, when  $\vec{M}$  is at its maximum height,  $\frac{\omega_2}{\gamma} \hat{2}G$  goes back to zero, the precession plane will again be a horizontal plane; however,  $\vec{M}$  no longer lies in this plane. In fact, if the instantaneous change in  $\frac{\omega_2}{\gamma} \hat{2}G$  rotated  $\vec{B}_{\text{eff}}$  by the angle  $\theta$ , then in the final condition  $\vec{M}$  will make an angle  $2\theta$  with the horizontal plane. Recall that the magnetometer senses the horizontal component of  $\vec{M}$ . Thus for the example above the signal has been reduced to have a peak amplitude of  $|\vec{M}| \cos 2\theta$ .

Conceivably this pattern of events could occur periodically; and  $\vec{M}$  would eventually become nearly coincident with the vertical axis. Such behavior was demonstrated with an analog simulation (Fig. III-7). For this simulation  $\gamma B_3$  was chosen as 1.0 rad/sec. The initial conditions were set to have  $\vec{M}(0) = |\vec{M}| \hat{I}G$  and  $\frac{\omega_2}{\gamma} \hat{2}G = 0$ . The  $\hat{2}G$  component of  $\vec{M}(t)$  was monitored at the analog console; then every time  $\vec{M}$  pointed along the  $\hat{2}G$  axis,  $\frac{\omega_2}{\gamma} \hat{2}G$  was made instantaneously  $\omega_2 \hat{2}G$  (for this example  $\omega_2 = 0.05$  rad/sec). Then when  $\vec{M}$  would point





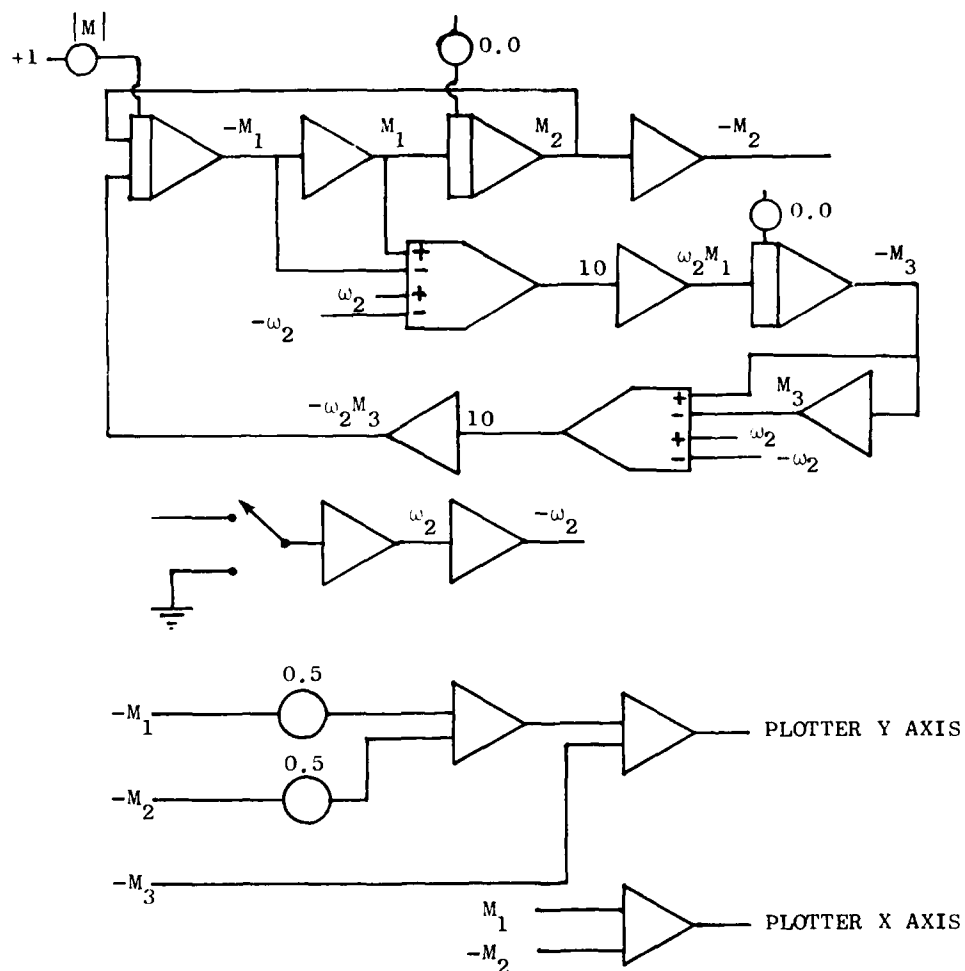


FIG. III-7 ANALOG SIMULATION FOR CROSS AXIS INPUTS. This is a simulation of Eq. (3.2) with  $\gamma B_3 = 1.0$  rad/sec and  $\omega_2 = 0.05$  rad/sec (or 0.0 rad/sec depending on the status of the switch). The initial conditions are set for  $\vec{M}(0) = |\vec{M}| \hat{i}$ .

along the  $-\hat{2G}$  axis,  $\vec{\omega}^{G-I}$  was instantaneously turned off. In this manner  $\vec{M}$  was brought into alignment with the vertical axis in about 245 sec (see Fig. III-8). The point here is that oscillatory behavior of  $\vec{\omega}^{G-I}$  near the resonance frequency can cause problems. Remember, however, that the second condition is that the change in direction of  $\vec{B}_{eff}$  be small compared to  $\gamma\vec{B}_{eff}$  to avoid this problem. Thus a small amplitude sinusoidal oscillation in  $\vec{\omega}^{G-I}$  at the resonance frequency will not cause as great a problem. Note also, though, that when the vertical component of  $\vec{\omega}^{G-I}$  is nearly equal and opposite to  $\gamma B_3$ ,  $\gamma\vec{B}_{eff}$  can be very small. Thus the resonance condition is not a constant but can be reduced (or increased) in frequency by a  $\hat{3G}$  component of  $\vec{\omega}^{G-I}$ .<sup>\*</sup> So in addition to wanting  $\gamma B_3 \geq 1/\sqrt{3} |\vec{\omega}^{G-I}|_{max}$  to resolve ambiguities, we have here another reason to scale the Larmor frequency well above the rotation rates we would expect the device to encounter in operation.

#### D. USE OF ADDITIONAL MAGNETIC FIELDS TO NULL CROSS AXIS INPUTS

It is clear from Fig. III-8 that some strategy must be employed to keep the magnetization in the precession plane despite the presence of cross axis rotations. We could consider restricting the operating regime to be always far away from resonance conditions; but there may be yet a more satisfactory approach. Consider again the Bloch equations for an arbitrary  $\vec{\omega}^{G-I}$ .

$$\frac{d}{dt} \begin{bmatrix} M_1 \\ M_2 \\ M_3 \end{bmatrix} = \begin{bmatrix} 0 & (\gamma B_3 + \omega_3) & -\omega_2 \\ -(\gamma B_3 + \omega_3) & 0 & \omega_1 \\ \omega_2 & -\omega_1 & 0 \end{bmatrix} \begin{bmatrix} M_1 \\ M_2 \\ M_3 \end{bmatrix}. \quad (3.14)$$

---

\* Professor DeBra has suggested deliberately introducing such a component by spinning the gyro about its input axis. This increases the effective Larmor frequency without introducing the field gradient problems that occur when the applied field is increased.

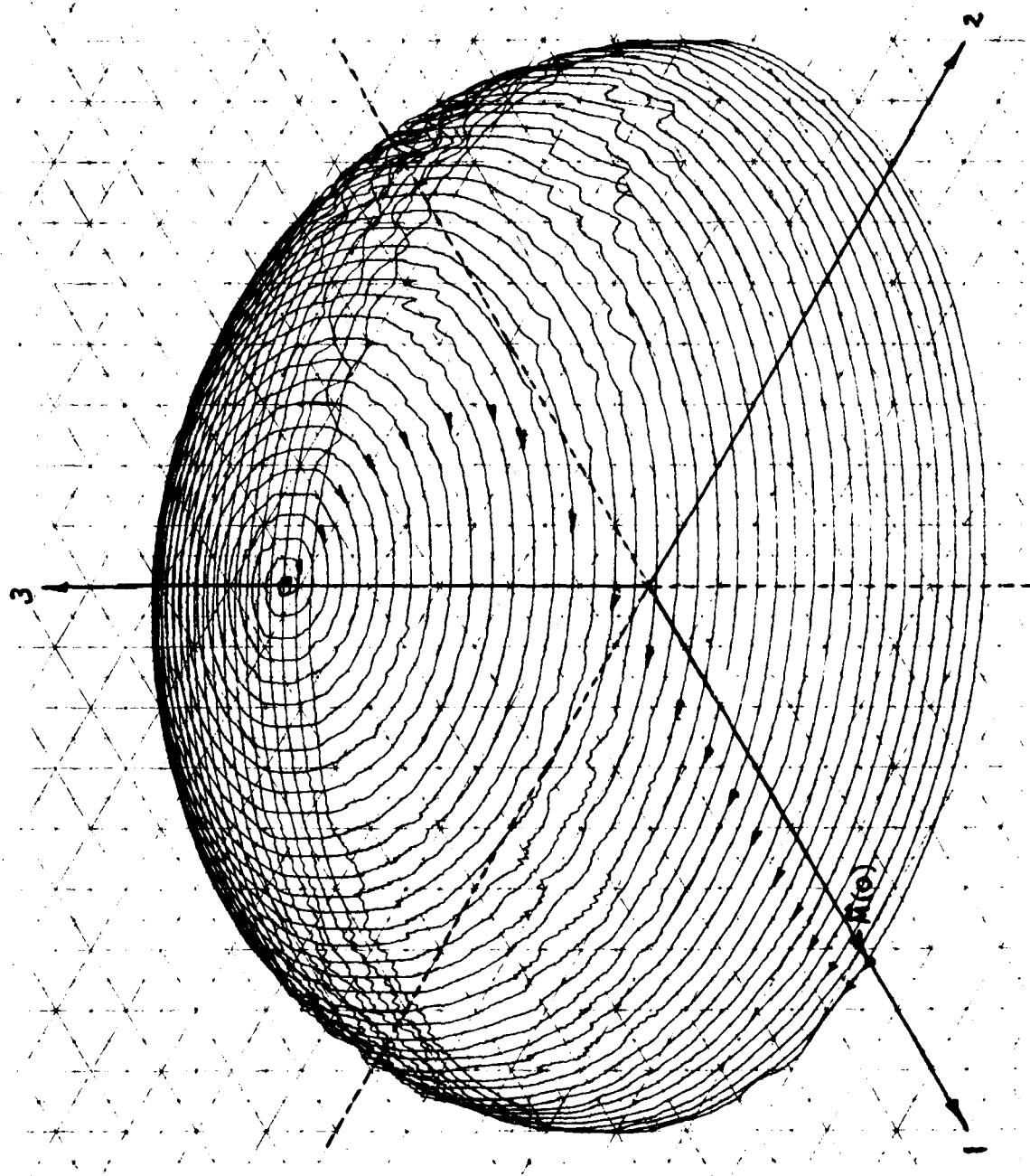


FIG. III-8 MAGNETIZATION TRAJECTORY WITH OSCILLATORY  $\omega_2$ .  
 Note that this simulation used a positive  $\gamma$ ; the precession direction for  $\text{He}^3$  would be opposite but the end result the same. The wiggles in the figure are due to rough plotter response.

If we add coils for generating magnetic fields in the  $\hat{1}G$  and  $\hat{2}G$  axes we get

$$\frac{d}{dt} \begin{bmatrix} M_1 \\ M_2 \\ M_3 \end{bmatrix} = \begin{bmatrix} 0 & (\gamma B_3 + \omega_3) & -(\gamma B_2 + \omega_2) \\ -(\gamma B_3 + \omega_3) & 0 & (\gamma B_1 + \omega_1) \\ (\gamma B_2 + \omega_2) & -(\gamma B_1 + \omega_1) & 0 \end{bmatrix} \begin{bmatrix} M_1 \\ M_2 \\ M_3 \end{bmatrix} \quad (3.15)$$

Thus if we can provide two control loops to keep both  $(\gamma B_1 + \omega_1)$  and  $(\gamma B_2 + \omega_2)$  zero, we can remove the effects of cross axis inputs.

#### E. THE THREE DEGREE-OF-FREEDOM GYRO

Since the nuclear gyro is sensitive to cross axis inputs, it is theoretically possible to determine all three components of  $\frac{\vec{\omega}^{G-I}}{\omega}$  with a single device. To do this three magnetometers are required, one to measure each component of  $\vec{M}$ . The procedure for determining  $\frac{\vec{\omega}^{G-I}}{\omega}$  from measurements of the components of  $\vec{M}$  is as follows:

- 1) Take three consecutive readings of  $\vec{M}$ ,  $\vec{M}_a$ ,  $\vec{M}_b$ , and  $\vec{M}_c$ .
- 2) Form the vectors  $\vec{M}_A = \vec{M}_b - \vec{M}_a$  and  $\vec{M}_B = \vec{M}_c - \vec{M}_a$ .
- 3) Assuming  $\frac{\vec{\omega}^{G-I}}{\omega}$  is constant during the three readings, then the vectors  $\vec{M}_A$  and  $\vec{M}_B$  lie in the precession plane and  $\frac{\vec{M}_A \times \vec{M}_B}{|\vec{M}_A| |\vec{M}_B|}$  is a unit vector in the direction  $-(\gamma B_1 + \omega_1) \hat{1}G - (\gamma B_2 + \omega_2) \hat{2}G - (\gamma B_3 + \omega_3) \hat{3}G$  which is denoted as  $\hat{n}$ .
- 4) Next choose any of the three measurements, say  $\vec{M}_b$ , and determine  $\vec{M}_b \times \hat{n} = |\vec{M}_b| \sin \phi$  or

$$\sin \phi = \frac{|\vec{M}_b \times \hat{n}|}{|\vec{M}_b|} \quad (3.16)$$

- 5) The radius of the precession plane is given by  $|\vec{M}_b| \sin \phi = |\vec{M}_b \times \hat{n}|$ .

- 6) Now  $|\vec{\omega}^{G-I}|$  can be determined (see Fig. III-9) from the radius of the precession plane, the time between measurements, and the measurements  $\vec{M}_a$  and  $\vec{M}_b$ .

$$\alpha = \cos^{-1} \frac{2|\vec{M}_b \times \hat{n}|^2 - |\vec{M}_c - \vec{M}_a|}{2|\vec{M}_b \times \hat{n}|^2}$$

$$|\vec{\omega}^{G-I}| = \alpha / \Delta t$$

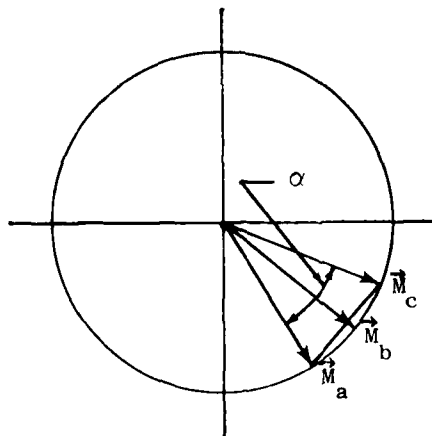


FIG. III-9 DETERMINATION OF  $\vec{\omega}^{G-I}$  FROM THREE MEASUREMENTS OF  $\vec{M}$ . The view is directly into the precession plane. Note  $\Delta t$  is the time between measurements  $\vec{M}_c$  and  $\vec{M}_a$ .

Assuming perfect measurements and no noise this scheme works very well. Figure III-10 shows two  $\vec{M}$  trajectories for a situation where a step change in  $\vec{\omega} - I$  occurs. In this case the size of the step is 10% of the Larmor frequency and is applied along the  $\hat{2G}$  axis at the time when  $\vec{M} = |\vec{M}| \hat{2G}$ . As can be seen, the precession plane tips down  $\sim 5.7$  deg (0.01 rad) with no control; but is visually unaffected when a magnetic field is applied to buck out the rotation. With control applied, the vertical component of the magnetization reaches only a value of  $-3.11 \times 10^{-8} |\vec{M}(0)|$ , and at a sample rate of 50 samples per Larmor period, the cross axis input is nulled after only three samples.

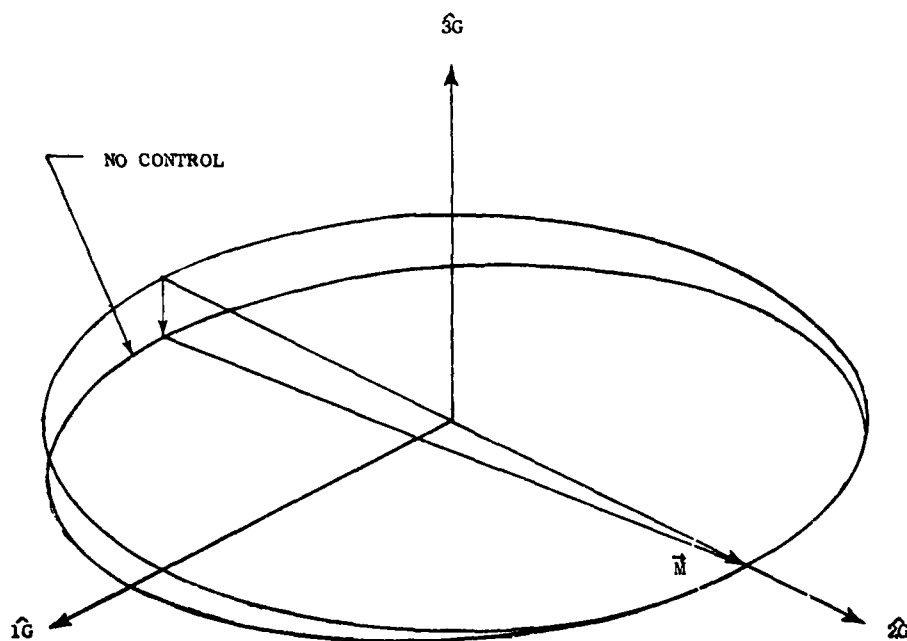


FIG. III-10 REMOVAL OF CROSS AXIS EFFECT WITH 3 DOF GYRO SCHEME. The horizontal precession plane is the plane for zero cross axis rate, the tilted precession plane is that for  $\omega_2 = 0.1 \gamma B_3 \hat{2G}$ . Use of 3 DOF gyro control scheme removes  $\omega_2$  effects leaving the initial horizontal precession plane virtually unchanged.

There are some problems with this approach. One is that the computation involved will limit the sample rate; but probably more crucial is the susceptibility to noise. Figure III-11 shows the source of the noise sensitivity. Here the first and third measurements are exact but the second is noisy. Since the algorithm to determine  $\vec{\omega}^{b-I}$  fits a circular precession plane to these three points, we see that the same amount of noise causes more problems for fast sample rates than for slow. So the measurement noise also places restrictions on the sample rate.

One final problem with this scheme should also be mentioned; and that is the effect of magnetometer drift on stability of the applied field. Since the SQUID magnetometers require a small, but finite current in the pickup coil, they will also generate magnetic fields. The effects of the pickup coil currents, transverse to the main field coil, will be small; but the pickup coil current in the same axis will add to the applied field directly. If this current were constant, its effect could be modeled out; however, a current change of  $1 \times 10^{-9}$  amps gives a drift of  $\sim 5 \times 10^{-5}$  rad/sec for the device in Ch. V.

#### F. THREE ORTHOGONAL SINGLE DEGREE-OF-FREEDOM (SDOF) GYROS

We now return to see what we can do with three orthogonal SDOF gyros each having one or two magnetometers orthogonal to each other (if two) and to the applied field axis. Since we now have added field coils in the cross axes to null cross axis rates, this is not the same problem as was investigated in Sect. III-B. These added field coils take out different components of the body rate for each of the three gyros. So while the solution for  $\vec{\omega}^{b-I}$  is still the intersection of three spheres the centers of the three spheres are no longer fixed. Just as the applied field moves the center of a given sphere along the negative input axis for that particular gyro, so too do the feedback fields move the center along the cross axes.

The question of ambiguities is not as clear here as it was for the case with no cross-axis field coils. However, one simple algorithm appears to work very well for determining  $\vec{\omega}^{b-I}$  from the three gyros.



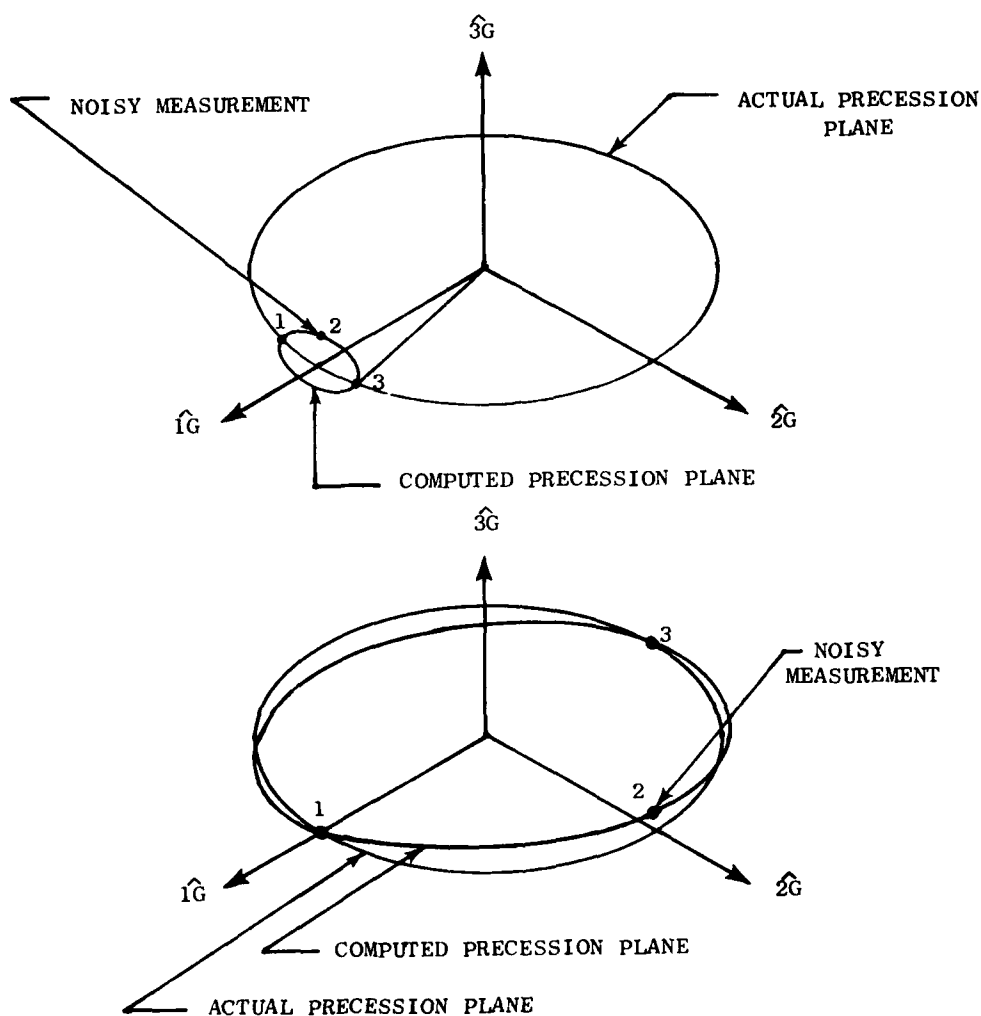


FIG. III-11 EFFECT OF MEASUREMENT NOISE ON 3 DOF GYRO SCHEME. The upper sketch shows the effect of a noisy measurement for a sample rate with respect to precession rate. The computed precession plane is orthogonal to the actual precession plane. The lower sketch shows the effect of the same amount of noise when the sample rate is slow. Here the actual and computed precession planes are nearly the same.

The procedure is as follows.

- 1) Measure the precession frequency for each gyro.
- 2) Compare this measured frequency with the zero input Larmor frequency and take the difference to be the rate about the input axis.
- 3) Use these estimated rates to determine the required cross axis fields.
- 4) Continue this procedure.

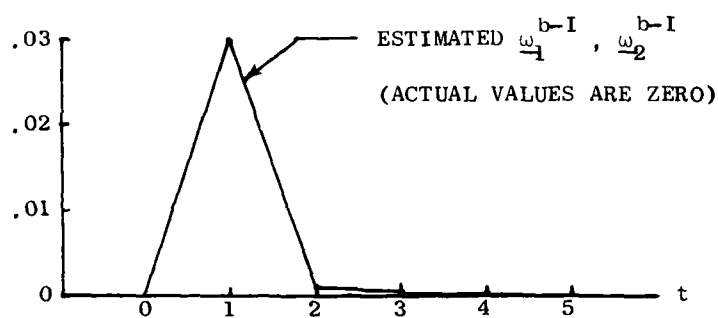
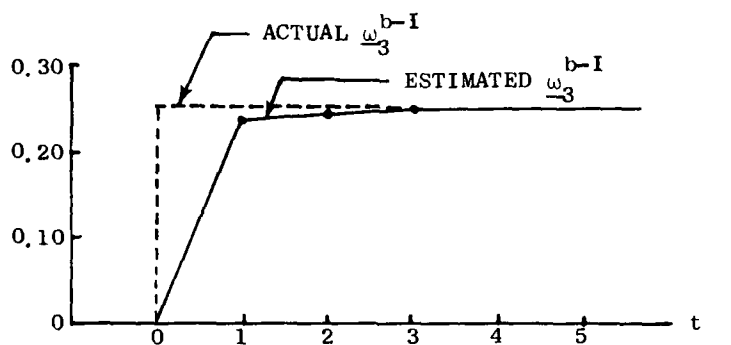
Figure III-12 shows the response to a step in  $\vec{\omega}^{b-I}$ . The step size is 25% of the Larmor frequency and is applied along the  $\hat{3b}$  axis. The significance to the time scale on Fig. III-12 is that the precession frequency of each gyro is assumed to be determined in one time unit. So let us look at what is involved in determining the precession frequency from the SQUID magnetometer(s) output. If one assumes that, during the measurement period, the precession frequency is constant and the gyro housing rotation rates are small compared to the Larmor frequency, then the SQUID output will be a sinusoidal signal, within a certain band, centered at the Larmor frequency. If the unwanted low- and high-frequency bands are filtered out then the SQUID output  $M_s(t)$  will have the form

$$M_s(t) = A \sin \omega t + B \cos \omega t. \quad (3.17)$$

Consider sampling this signal at a fixed sample period,  $T$  sec. Then it is shown that the  $n$ th sample is given by

$$\begin{aligned} M_s(n) = & B\delta(T) + (A \sin \omega T - B \cos \omega T)\delta(T-1) \\ & + 2 \cos \omega T M_s(n-1) - M_s(n-2). \end{aligned} \quad (3.18)$$

We can write this out in matrix form as



$$|\omega_3^{b-I}| = \begin{cases} 0 & \text{for } t < 0 \\ 0.25 \hat{\omega} & \text{for } t \geq 0 \end{cases}$$

FIG. III-12 RESPONSE TO A STEP IN  $\omega^{b-I}$ . Note one unit of time is the time required to measure the precession frequencies in all three gyros.

$$\begin{bmatrix} M_s(0) \\ M_s(1) \\ M_s(2) \\ M_s(3) \\ M_s(4) \\ \vdots \end{bmatrix} = \begin{bmatrix} 1 & 0 & 0 & 0 \\ 0 & 1 & M_s(0) & 0 \\ \hline 0 & 0 & M_s(1) & M_s(0) \\ 0 & 0 & M_s(2) & M_s(1) \\ 0 & 0 & M_s(3) & M_s(2) \\ \vdots & \vdots & \vdots & \vdots \end{bmatrix} \begin{bmatrix} B \\ A \sin \omega T - B \cos \omega T \\ 2 \cos \omega T \\ -1 \end{bmatrix} \quad (3.19)$$

The upper left partition is due to initial conditions so if we wait two sample periods we have

$$\underbrace{\begin{bmatrix} M_s(2) \\ M_s(3) \\ M_s(4) \\ \vdots \end{bmatrix}}_y = \underbrace{\begin{bmatrix} M_s(1) & M_s(0) \\ M_s(2) & M_s(1) \\ M_s(3) & M_s(2) \\ \vdots & \vdots \end{bmatrix}}_A \underbrace{\begin{bmatrix} 2 \cos \omega T \\ -1 \end{bmatrix}}_a \quad (3.20)$$

Now define  $2 \cos \omega T = a_1$  and  $-1 = a_2$  and consider the case where we have noise  $v$  such that

$$y = Aa + v \quad (3.21)$$

We know, via measurements, both  $y$  and  $A$ ; and we can get a best least squares estimate of  $a$  as

$$\hat{a} = (A^T A)^{-1} A^T y \quad (3.22)$$

Since we know  $a_2 = -1$  we could consider the convergence of  $\hat{a}_2$  to  $-1$

as a simple test for a good estimate of  $a_1$ . Finally, we estimate the precession frequency from  $\hat{a}_1$  as

$$\hat{\omega} = \frac{1}{T} \cos^{-1} \left( \frac{\hat{a}_1}{2} \right) .$$

Then the estimates of  $\omega$ , one for each gyro, can be used to determine the fields necessary to cancel the cross axis rates. Note that if fields are generated, there will be changes in the precession frequencies of the three gyros. Thus the next two samples will again exhibit the transient terms in (3.19).

## Chapter IV

### KINEMATIC RECTIFICATION

#### A. STATEMENT OF THE PROBLEM

One rectification mechanism has been discussed in Ch. III, i.e., the rectification of cross axis rates. It was seen that a cross axis rate increased the precession frequency independent of the sign of the cross axis rate. Thus oscillatory cross axis rate inputs will produce an average drift even if the average cross axis rate is zero. Another well known rectification drift for SDOF gyros is kinematic rectification [Cannon 1957]. The mechanism for kinematic induced drift, as it applies to the He<sup>3</sup> nuclear gyro is investigated here.

Consider the situation shown in Fig. IV-1. The I-frame is an inertial frame and the G-frame is the He<sup>3</sup> gyro frame. Assume that the applied field is along the  $\hat{3G}$  axis and that  $\theta_1$  and  $\theta_2$  are driven such as to maintain a constant angle  $\beta$  between the  $\hat{3G}$  and  $\hat{3I}$  axes as the  $\hat{3G}$  axis cones around the  $\hat{3I}$  axis at a frequency  $\omega_z$  rad/sec. Then

$$\vec{\omega}^{G-I} = \dot{\theta}_1 \hat{1G} + \dot{\theta}_2 \hat{2I} \quad (4.1)$$

$$\vec{\omega}^{G-I} = \dot{\theta}_1 \hat{1G} + \dot{\theta}_2 \cos \theta_1 \hat{2G} - \theta_2 \sin \theta_1 \hat{3G} . \quad (4.2)$$

Thus if the gimbal angles are given by

$$\theta_1(t) = -\beta \cos \omega_z t \quad (4.3a)$$

$$\theta_2(t) = \beta \sin \omega_z t \quad (4.3b)$$

then for small angles  $\sin \theta_1 \approx \theta_1$  and we see the component about the  $\hat{3G}$  axis is approximately given by

$$-\dot{\theta}_2 \sin \theta_1 \approx -\dot{\theta}_2 \theta_1 = -\beta^2 \omega_z \cos^2 \omega_z t . \quad (4.4)$$

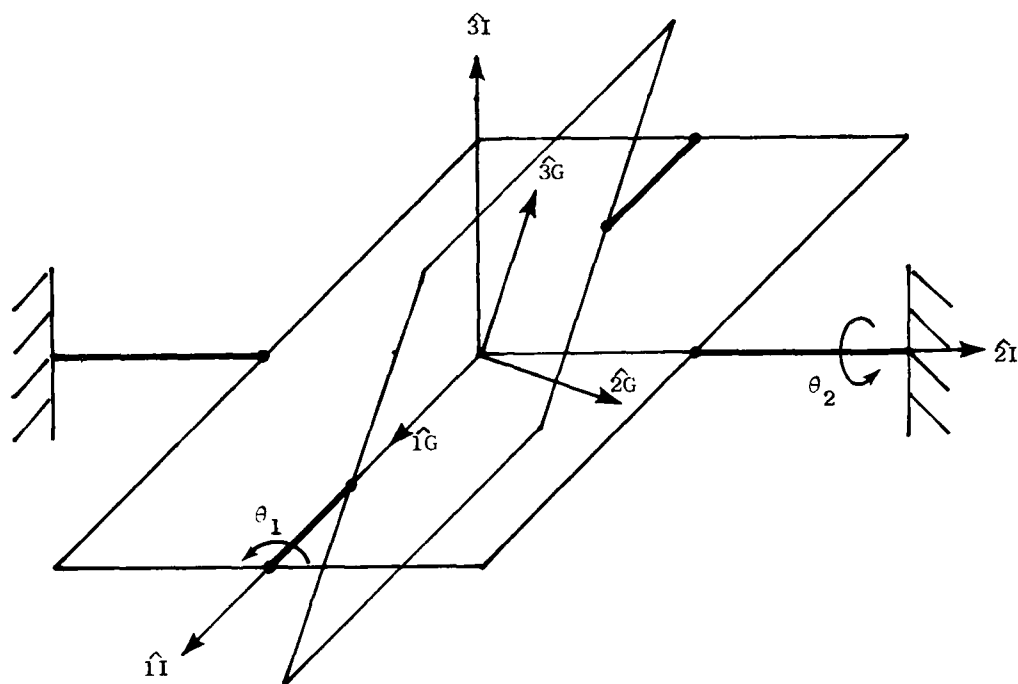


FIG. IV-1 INPUT AXIS CONING OF A SINGLE DEGREE OF FREEDOM (SDOF) GYRO. Angles  $\theta_1$  and  $\theta_2$  are driven to cause the  $\hat{3G}$  axis to cone about the  $\hat{3I}$  axis, at a frequency  $\omega_2$ , while maintaining a constant angle  $\beta$  between the two axes.

This component has an average value despite the fact that the gyro has no average displacement about the  $\hat{3G}$  axis with respect to the inertial frame. Since the gyro is intended to measure the  $\hat{3G}$  component of  $\vec{\omega} - \vec{1}$  though we expect to see  $(-\dot{\theta}_2 \theta_1)_{\text{avg}}$  as the gyro output. This is the drift due to kinematic rectification and is given by

$$(-\dot{\theta}_2 \theta_1)_{\text{avg}} = -\frac{1}{2} \dot{\theta}_2 \theta_1 \quad (4.5)$$

$$= -\frac{1}{2} \beta^2 \omega_z \quad (4.6)$$

And so this term is seen to depend on the cone half angle  $\beta$  and the frequency of the coning,  $\omega_z$ . Note that nothing has been assumed about the nature of the gyro itself other than it is a single degree-of-freedom gyro. Thus one would expect to see this behavior in all single DOF gyros. Indeed, it has been observed in conventional mechanical gyros and also laser gyros. To date no attempt has been made to observe kinematic rectification in nuclear gyros. Chapter V will describe an experiment design to make this observation.

#### B. ANALYSIS OF KINEMATIC RECTIFICATION EFFECTS FOR THE $\text{He}^3$ GYRO

We can solve for the effects of coning motion for the nuclear gyro using the Bloch equations and assuming relaxation effects can be neglected. This problem is most easily solved in a rotating frame where the applied field,  $\vec{B} = B_3 \hat{3G}$ , is constant (see Fig. IV-2). This rotating or R-frame rotates at the coning frequency,  $\omega_z$ , about the  $\hat{3R}$  axis. So in this frame the applied field is constant and is given by

$$\vec{B}_R = B_3 \sin \beta \hat{1R} + B_3 \cos \beta \hat{3R} \quad (4.7)$$

$$= B_1 \hat{1R} + B_z \hat{3R} \quad (4.8)$$



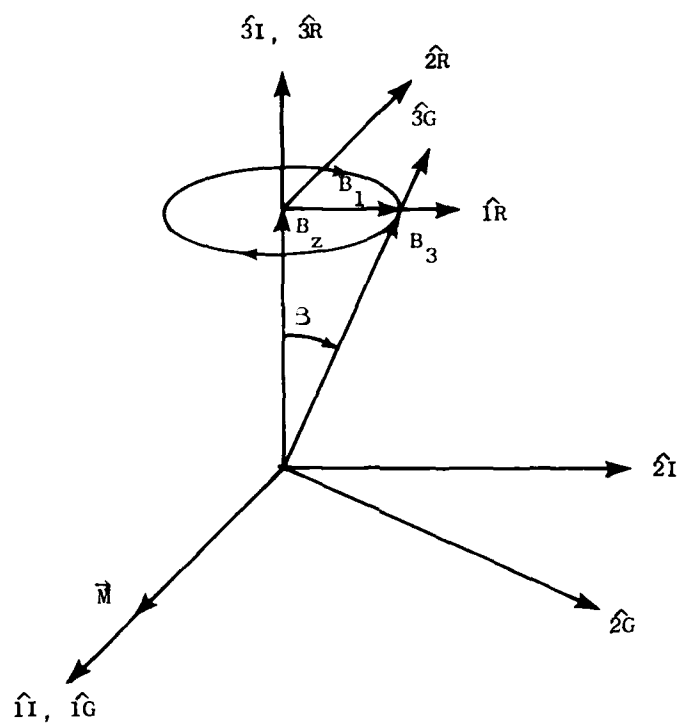


FIG. IV-2 REFERENCE FRAMES FOR KINEMATIC RECTIFICATION ANALYSIS. The rotating R-frame rotates at the coning frequency  $\omega_z$  around the  $\hat{3}I$  axis such that  $B_1$  always points along the  $\hat{1}R$  axis.

Then the equation of motion for  $\vec{M}$  in the R-frame is

$$\frac{d}{dt} \vec{M} = \frac{\vec{I}}{\omega} \times \vec{M} \quad (4.9)$$

Writing out the components in the R-frame we have

$$\frac{d}{dt} \begin{bmatrix} M_1 \\ M_2 \\ M_3 \end{bmatrix} = \begin{bmatrix} 0 & (\gamma B_z - \omega_z) & 0 \\ -(\gamma B_z - \omega_z) & 0 & \gamma B_1 \\ 0 & -\gamma B_1 & 0 \end{bmatrix} \begin{bmatrix} M_1 \\ M_2 \\ M_3 \end{bmatrix} \quad (4.10)$$

Finally we solve for  $\vec{M}$  in the R-frame to get

$$\vec{M}(t) = \mathcal{L}^{-1} \left\{ \left( sI - \begin{bmatrix} 0 & (\gamma B_z - \omega_z) & 0 \\ -(\gamma B_z - \omega_z) & 0 & \gamma B_1 \\ 0 & -\gamma B_1 & 0 \end{bmatrix} \right)^{-1} \right\} \vec{M}(0) \quad (4.11)$$

$$\vec{M}(t) = \begin{bmatrix} \cos \omega t + \left( \frac{\gamma B_1}{\omega} \right)^2 (1 - \cos \omega t) & \frac{\gamma B_z - \omega_z}{\omega} \sin \omega t & \frac{\gamma B_1 (\gamma B_z - \omega_z)}{\omega^2} (1 - \cos \omega t) \\ -\frac{\gamma B_z - \omega_z}{\omega} \sin \omega t & \cos \omega t & \frac{\gamma B_1}{\omega} \sin \omega t \\ \frac{\gamma B_1 (\gamma B_z - \omega_z)}{\omega^2} (1 - \cos \omega t) & -\frac{\gamma B_1}{\omega} \sin \omega t & \cos \omega t + \left( \frac{\gamma B_z - \omega_z}{\omega} \right)^2 (1 - \cos \omega t) \end{bmatrix} \vec{M}(0) \quad (4.12)$$

where

$$\omega = \sqrt{(\gamma B_1)^2 + (\gamma B_z - \omega_z)^2} \quad (4.13)$$

Now if Fig. IV-2 depicts the initial conditions, then  $\vec{M}(0) = -|\vec{M}| \hat{R}$  and the solution is

$$M_1(t) = - |\vec{M}| \frac{(\gamma B_z - \omega_z)}{\omega} \sin \omega t \quad (4.14a)$$

$$M_2(t) = - |\vec{M}| \cos \omega t \quad (4.14b)$$

$$M_3(t) = |\vec{M}| \frac{\gamma B_1}{\omega} \sin \omega t . \quad (4.14c)$$

We now make use of the transformation

$$\begin{bmatrix} \hat{1}I \\ \hat{2}I \\ \hat{3}I \end{bmatrix} = \begin{bmatrix} \sin \omega_z t & -\cos \omega_z t & 0 \\ \cos \omega_z t & \sin \omega_z t & 0 \\ 0 & 0 & 1 \end{bmatrix} \begin{bmatrix} \hat{1}R \\ \hat{2}R \\ \hat{3}R \end{bmatrix} \quad (4.15)$$

the solution in I-frame coordinates becomes

$$M_1(t) = - |\vec{M}| \left[ \frac{(\gamma B_z - \omega_z)}{\omega} \sin \omega t \sin \omega_z t - \cos \omega t \cos \omega_z t \right] \quad (4.16a)$$

$$M_2(t) = - |\vec{M}| \left[ \frac{(\gamma B_z - \omega_z)}{\omega} \sin \omega t \cos \omega_z t + \cos \omega t \sin \omega_z t \right] \quad (4.16b)$$

$$M_3(t) = |\vec{M}| \frac{\gamma B_1}{\omega} \sin \omega t . \quad (4.16c)$$

Now if we look at the  $M_1(t)$  component in the I-frame we can simplify (4.16a) to get

$$M_1(t) = - \frac{|\vec{M}|}{2} \left\{ \frac{\gamma B_z - \omega_z - \omega}{\omega} \cos(\omega - \omega_z)t - \frac{\gamma B_z - \omega_z + \omega}{\omega} \cos(\omega + \omega_z)t \right\} . \quad (4.17)$$

In as much as the  $\hat{1}G$  axis never gets far from the  $\hat{1}I$  axis, then if the coning motion produced no effect, a magnetometer in the  $\hat{1}G$  axis would see a signal that, on the average, looked like  $|\vec{M}| \cos \gamma B_3 t$ . Equation (4.17), however, shows that this is not the case. The question now is does the deviation from  $|\vec{M}| \cos \gamma B_3 t$  agree with drift term we would expect from kinematic rectification. Table IV-1 shows a variety

of conditions comparing the drift rate calculated from (4.17) with that predicted from (4.6).

Table IV-1  
COMPARISON OF DRIFT PREDICTED BY ANALYSIS WITH  
CLASSICAL KINEMATIC RECTIFICATION DRIFT

| $\gamma B_3 = 1.0 \text{ rad/sec}; \quad \beta = 0.5 \text{ deg}$ |                                  |   |
|---|----------------------------------|---|
| $\omega_z$  | Drift Predicted by<br>Eq. (4.17) | Drift Predicted by Classical<br>Kinematic Rectification (Eq. 4.6) |
| <u>(rad/sec)</u>  | <u>(rad/sec)</u>                 | <u>(rad/sec)</u>  |
| 0   | 0                                | 0   |
| $1 \times 10^{-4}$  | $4.0 \times 10^{-9}$             | $4.0 \times 10^{-9}$  |
| $1 \times 10^{-3}$  | $3.8 \times 10^{-8}$             | $3.8 \times 10^{-8}$  |
| $1 \times 10^{-2}$  | $3.85 \times 10^{-7}$            | $3.81 \times 10^{-7}$   |
| $5 \times 10^{-2}$  | $2.00 \times 10^{-6}$            | $1.90 \times 10^{-6}$   |
| $1 \times 10^{-1}$  | $4.23 \times 10^{-6}$            | $3.81 \times 10^{-6}$   |
| $5 \times 10^{-1}$  | $3.81 \times 10^{-5}$            | $1.90 \times 10^{-5}$   |
| $7 \times 10^{-1}$  | $8.88 \times 10^{-5}$            | $2.67 \times 10^{-5}$   |
| $9 \times 10^{-1}$  | $3.42 \times 10^{-4}$            | $3.43 \times 10^{-5}$   |
| $9.9 \times 10^{-1}$  | $3.24 \times 10^{-3}$            | $3.77 \times 10^{-5}$   |
| $\gamma B_3 \cos \beta$   | $8.69 \times 10^{-3}$            | $3.81 \times 10^{-5}$   |

Table IV-1 shows good agreement between the analysis and the classical kinematic rectification drift up to an  $\omega_z$  which is about 10% of the Larmor frequency. For  $\omega_z > 0.1\gamma B_3$ , the drift predicted from (4.17) is greater than would be predicted from the kinematic rectification effect alone. Part of this increase is due to cross axis rate rectification. Since the precession rate is the square root of the sum of the squares of each component, we must consider the average squared values of the cross axis rates. So combining these two rectification mechanisms,

we could predict the magnitude of the precession rate, PR, to be

$$PR = \sqrt{(\gamma B_3 + \frac{1}{2}P^2\omega_z)^2 + \frac{1}{2}(P\omega_z)^2 + \frac{1}{2}(P\omega_z)^2} \quad (4.18)$$

By including the cross axis rate rectification effect, we do get better agreement with the analysis; but even in this case agreement is not good as we approach the resonance condition ( $\omega_z = \gamma B_3 \cos \beta$ ). Table IV-2 summarizes these results.

Table IV-2  
COMPARISON OF DRIFT PREDICTED BY  
EQS. (4.17) and (4.18)

| $\gamma B_3 = 1.0 \text{ rad/sec}; \quad \beta = 0.5 \text{ deg}$ |                                |                                |
|---|--------------------------------|--------------------------------|
| $\omega_z$<br>(rad/sec)   | Drift from (4.17)<br>(rad/sec) | Drift from (4.18)<br>(rad/sec) |
| $1 \times 10^{-4}$  | $4.0 \times 10^{-9}$           | $4.0 \times 10^{-9}$           |
| $1 \times 10^{-3}$  | $3.8 \times 10^{-8}$           | $3.8 \times 10^{-8}$           |
| $1 \times 10^{-2}$  | $3.85 \times 10^{-7}$          | $3.85 \times 10^{-7}$          |
| $1 \times 10^{-1}$  | $4.23 \times 10^{-6}$          | $4.19 \times 10^{-6}$          |
| $5 \times 10^{-1}$  | $3.81 \times 10^{-5}$          | $2.86 \times 10^{-5}$          |

To understand why the drift rate given by (4.17) is still greater than that predicted by (4.18) as resonance is approached, consider what happens at resonance. At the resonance condition the rotating component of the applied field rotates about the  $\hat{3I}$  axis at the same rate that the magnetization vector precesses about it. For the initial conditions shown in Fig. IV-2,  $\vec{M}$  will precess around the stationary component of the field at a rate  $\gamma B_3 \cos \beta$  rad/sec. Since  $B_1$  also remains perpendicular to  $\vec{M}$  as  $\vec{M}$  precesses about the static field,  $\vec{M}$  will also

precess about  $B_1$  at a rate  $\gamma B_3 \sin \beta$  rad/sec. These two precessions occur simultaneously so both sum and difference frequencies are observed. Coming into resonance for the particular initial conditions chosen here we see the sum of the two frequencies, namely  $(\gamma B_3 \cos \beta + \gamma B_3 \sin \beta)$  rad/sec, which, for the conditions used to generate Tables IV-1 and IV-2, is 1.00869 rad/sec. Thus we get the drift term  $8.69 \times 10^{-3}$  rad/sec. Had we chosen for our initial conditions a situation which had  $B_1$  and  $\vec{M}$  parallel, we would have a precession frequency of  $\gamma B_3 \cos \beta$  rad/sec at resonance, because the rotating  $B_1$  would have no influence on  $\vec{M}$ .

### C. FREQUENCY DEPENDENCE

At this point we have built a good case for a classical kinematic rectification drift effect for the  $\text{He}^3$  nuclear gyro. We have, however, only examined cases for which  $\omega_z$  was in the same direction as, and no greater than, the Larmor precession. As we pass beyond the resonance condition another mechanism takes over. Referring to (4.17), it may be shown that from  $\omega_z = 0$  to just below resonance, the coefficient of the  $\cos(\omega + \omega_z)t$  term is approximately 2 while that of the  $\cos(\omega - \omega_z)t$  term is nearly zero. The opposite is true beyond resonance and the former is nearly zero while the latter is about -2 (at resonance the first is -1.0; the second is 1.0). Table IV-3 shows the drift for coning frequencies above the resonance condition. Note that coming out of resonance ( $\omega_z = 1.0$  rad/sec) the precession frequency is nearly  $(\gamma B_3 \cos \beta - \gamma B_3 \sin \beta)$  which would give a drift rate of  $-8.76 \times 10^{-3}$  rad/sec.

The region above resonance is characterized by a drift rate opposite in direction to the drift rate below resonance and asymptotically approaching  $-3.81 \times 10^{-5}$  rad/sec. It may seem strange that the drift rate should change signs when both the kinematic rectification and cross axis rate rectification effects predict a steadily increasing positive drift rate with increasing  $\omega_z$ . However, what has happened is that these effects no longer apply. Recall from the discussion in the previous chapter that when the direction of the effective field changes slowly, the precession plane is able to follow, and  $\vec{M}$  remains in the precession plane.

Table IV-3  
DRIFT RATES FOR  $\omega_z$  ABOVE RESONANCE

| $\gamma B_3 = 1.0;$ $\beta = 0.5 \text{ deg}$ |                                     |
|---|-------------------------------------|
| $\omega_z$<br>(rad/sec)                       | Drift Rate From (4.17)<br>(rad/sec) |
| 1.0   | $-8.73 \times 10^{-3}$              |
| 5.0   | $-4.76 \times 10^{-5}$              |
| 10.0  | $-4.23 \times 10^{-5}$              |
| 50.0  | $-3.89 \times 10^{-5}$              |
| 100.0   | $-3.85 \times 10^{-5}$              |
| 500.0   | $-3.82 \times 10^{-5}$              |

When this is the case the  $\text{He}^3$  nuclei behave as if they were gimbaled, and their spin axes follow the applied field as it cones about. In this regime (4.18) applies. As the coning frequency increases, however, the magnetization vector cannot stay in the precession plane. Then at sufficiently high frequencies the  $\text{He}^3$  nuclei do not respond to the rotating component of the applied field at all, and they become, in effect, uncoupled from the coning motion of the gyro case. Why then the drift? The answer is that since the applied field is made up of both a rotating and a static component; and for  $\omega_z \gg \gamma B_3 \cos \beta$  the  $\text{He}^3$  responds only to the static component, the precession frequency will approach  $\gamma B_3 \cos \beta$ . Thus it is slower than the Larmor frequency, and in the limit approaches a drift rate of  $(\gamma B_3 \cos \beta - \gamma B_3)$ , which for the conditions in the tables is  $-3.81 \times 10^{-5} \text{ rad/sec}$ .

Figure IV-3 shows the magnitude of the drift vs the coning frequency for  $\gamma B_3 = 1.0 \text{ rad/sec}$  and  $\beta = 0.5 \text{ deg}$ . The solid curve is for  $\omega_z$  opposite in direction to the Larmor precession, and the dashed curve represents the case where the directions are the same. Note that the resonance condition applies only in the latter case.

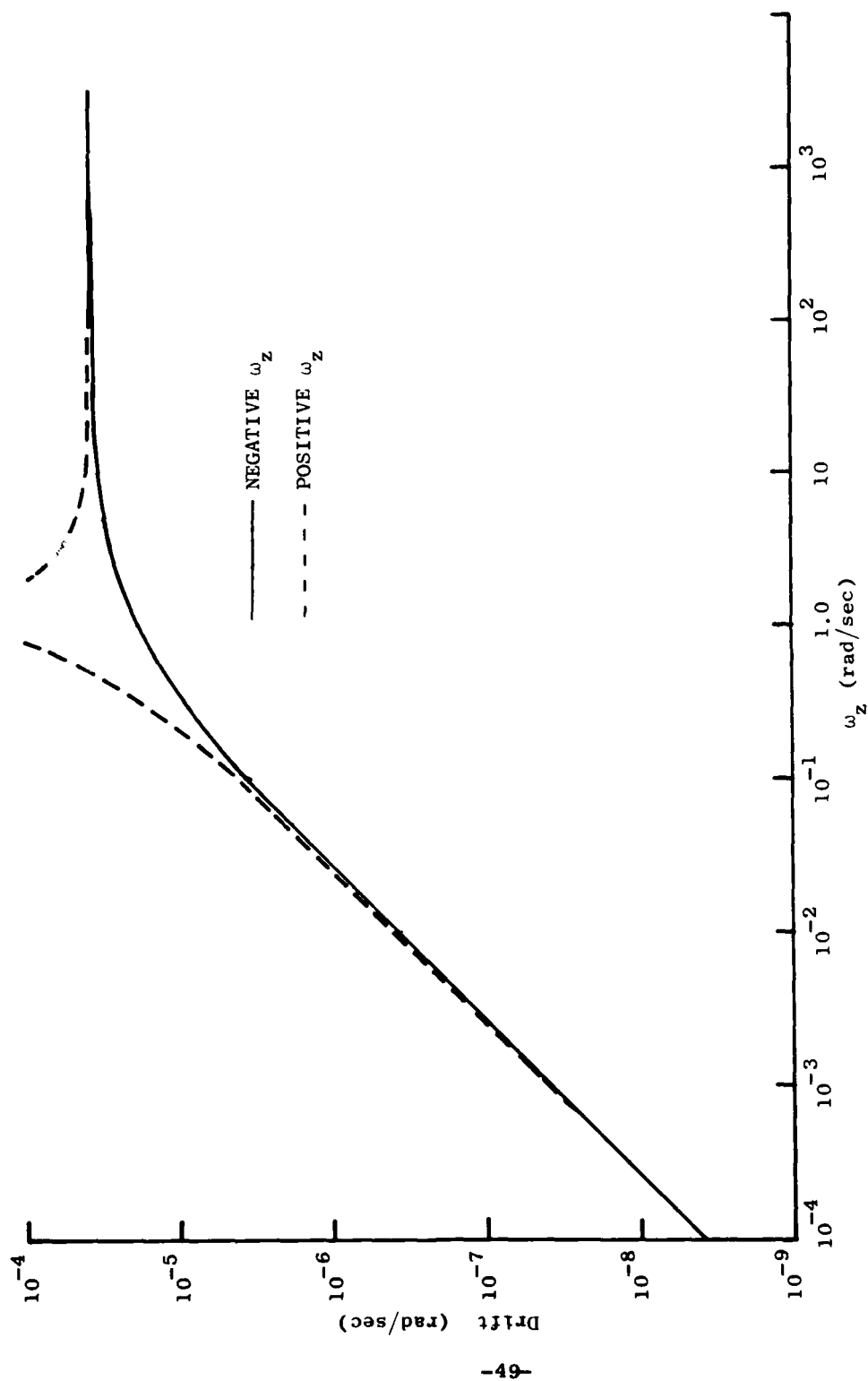


FIG. IV-3 DRIFT VS CONING FREQUENCY ( $\gamma B_3 = 1.0$  rad/sec;  $\beta = 0.5$  deg).



We can see at the low coning frequencies,  $|\omega_z| \leq 0.5 |\gamma B_3|$ , that the dominant effects are the two rectification mechanisms; Eq. (4.18) gives good results in this range. Then as  $\omega_z$  increases in magnitude either resonance or uncoupling from the motion sets in and (4.17) must be used. Finally, in the limit of large  $\omega_z$  the  $\text{He}^3$  nuclei do not respond to the  $B_1$  component of the field and the drift rate approaches  $-3.81 \times 10^{-5}$  rad/sec. Figure IV-4 summarizes the regions of influence for the case where  $\beta = 0.5$  deg.

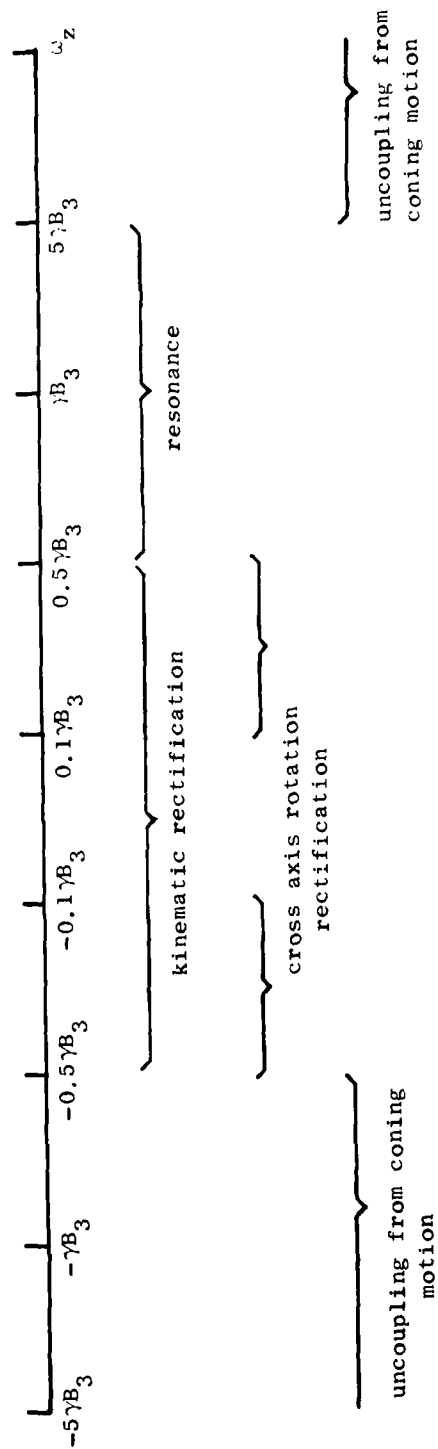


FIG. IV-4 REGIONS OF INFLUENCE. Here  $\beta = 0.5$  deg.

Chapter V  
AN EXPERIMENT TO MEASURE KINEMATIC  
RECTIFICATION EFFECTS

A. OBJECTIVE

Because of the nonconventional behavior with regard to kinematic rectification, it was desired that some experimental verification be performed. In particular, the experiment should be designed to accomplish the following.

- a) Verify the frequency dependence of both kinematic and cross axis rate rectification mechanisms by varying the coning frequency.
- b) Separate kinematic from cross axis rate rectification effects by changing the sign of  $\omega_z$ .
- c) Verify the uncoupling from the coning motion at high  $\omega_z$ .

B. LABORATORY FACILITIES

As discussed previously, Taber [Taber 1978] had performed extensive experiments measuring the longitudinal relaxation times of polarized  $\text{He}^3$ . Thus there already existed a cryogenic facility for performing  $\text{He}^3$  nuclear gyro experiments (see Fig. V-1). Furthermore, the cryostat probe used for the relaxation time experiments (Fig. V-2) was still available.

Longitudinal relaxation times,  $T_1$ , of 140 hours had been obtained with this device [Taber 1978] using a liquid sample of 0.07%  $\text{He}^3$  in  $\text{He}^4$  solution. Transverse relaxation times,  $T_2$ , have not been measured; but since we will now have a lower ambient magnetic field ( $\sim 2 \times 10^{-8}$  G or  $2 \times 10^{-12}$  T) and will remove the magnetic contaminant that was present for the earlier  $T_1$  measurements, we can expect  $T_2$  to be of the same

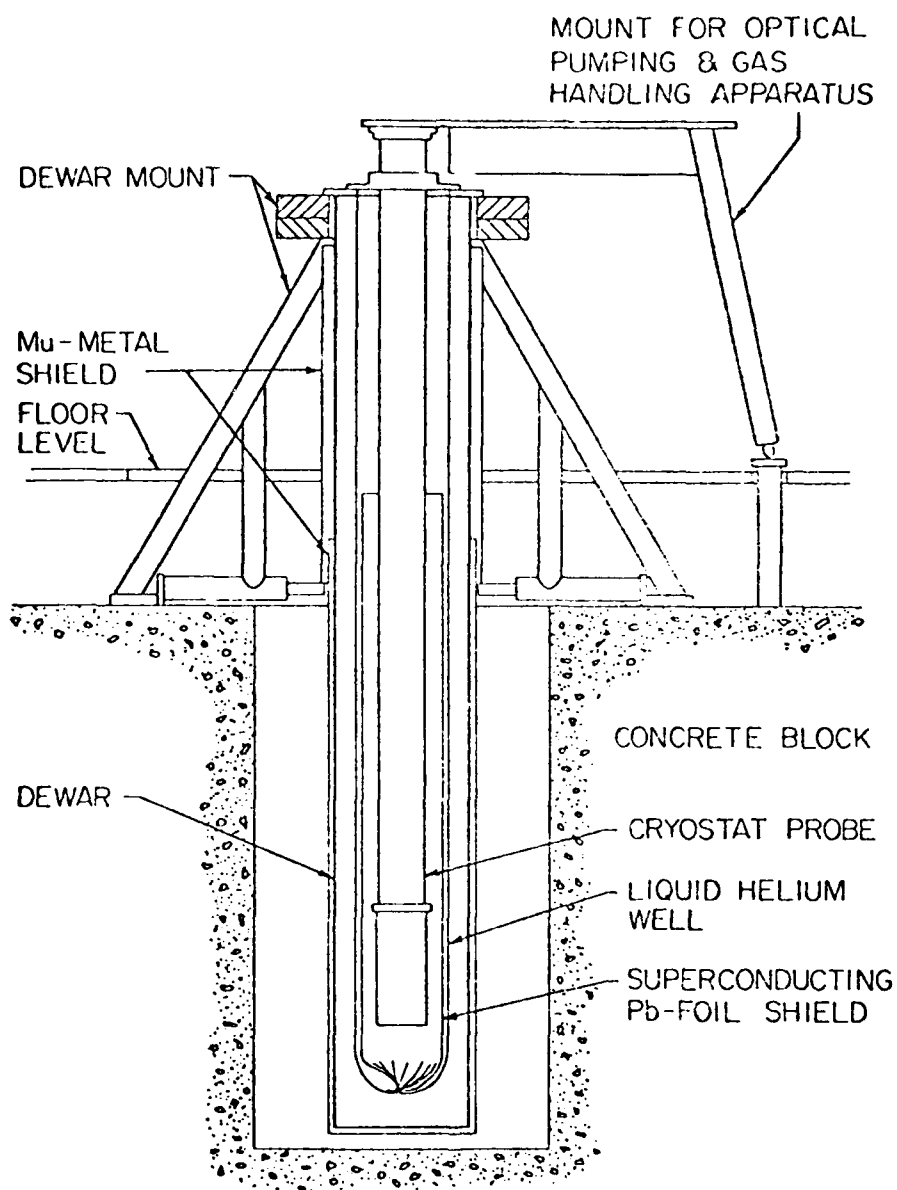


FIG. V-1 GENERAL EXPERIMENTAL CONFIGURATION. Not shown are the field coils for the optical pumping, the optical pumping apparatus and the gas-handling apparatus. [From Taber 1978.]

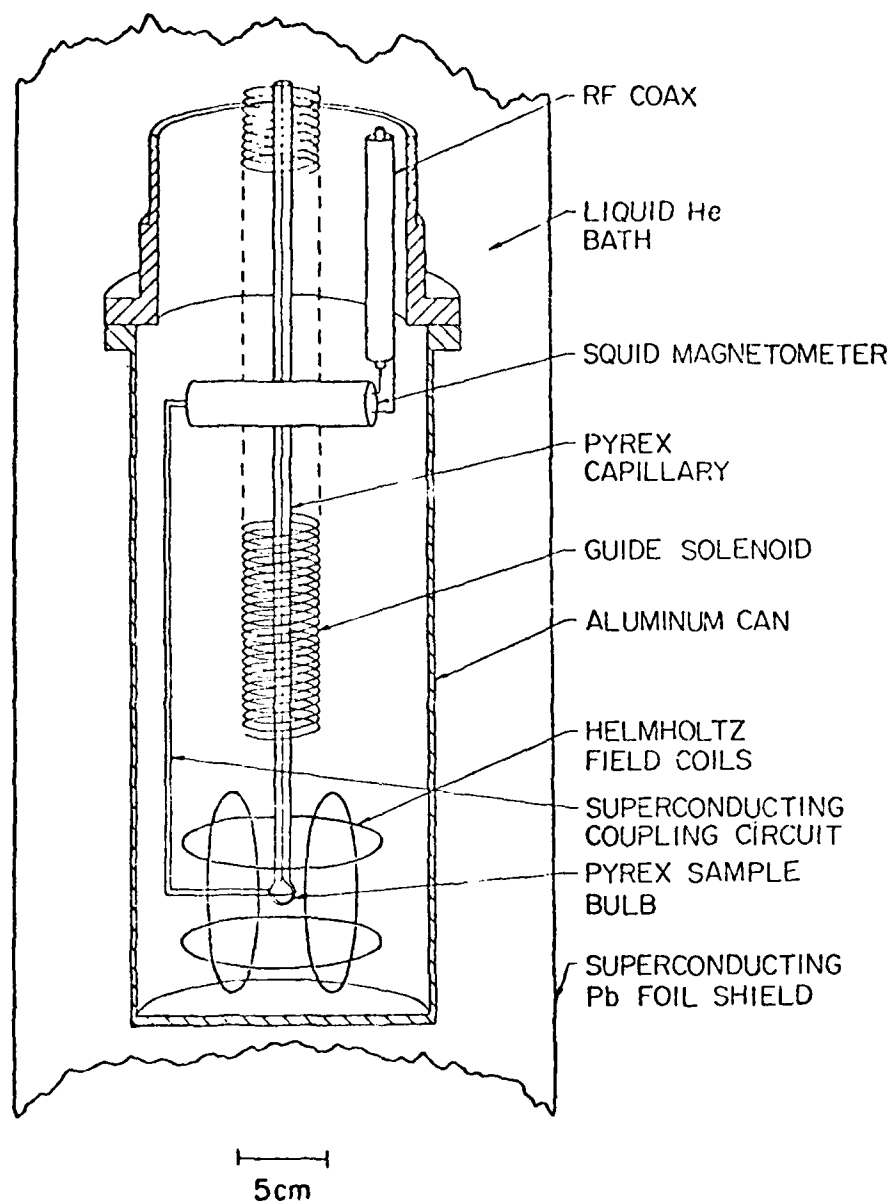


FIG. V-2 SCHEMATIC DEPICTION OF THE BOTTOM PORTION OF THE CRYOSTAT PROBE [from Taber 1978].

order of magnitude as the  $T_1$  measurement. Further, by carefully metering the flow of the polarized  $\text{He}^3 - \text{He}^4$  mixture into the sample cell, a uniform cell wall coating of frozen hydrogen can be maintained. This will reduce the relaxation due to wall collisions [Taber 1978] thus increasing both  $T_1$  and  $T_2$ . So it looks very promising that  $T_2$  should be sufficiently long to perform the desired experiments.

There were, however, some problems with the existing experimental configuration. The first was that the probe had only two orthogonal field coils. The second was that the material used to construct the coil forms, delrin, was not sufficiently free of ferromagnetic contaminants. Both of these problems were solved by redesigning that portion of the device. Corning Macor, a machinable glass ceramic, was chosen as the material for the coil forms. Samples of this material were found to be magnetically cleaner than similar samples of delrin [Cabrera 1975].

One final problem was that for the given experimental configuration mechanical inputs are difficult. The gyro is located in the cryostat probe which is lowered into the dewar; and only limited rotation around the vertical axis is possible.

#### C. BASIC CONCEPT

Since a controlled mechanical coning motion is not feasible, the experiment can be performed utilizing the equivalence between mechanical rotations and applied magnetic fields. Thus instead of physically coning the gyro input axis, the rotating component of the magnetic field is generated with the coils in the  $\hat{1}G$  and  $\hat{2}G$  axes. Then since the gyro will not be subject to any rotations (except earth rotation) we can consider it to represent the I-frame; and thus a magnetometer located in the  $\hat{1}G$  axis will sense the  $M_1(t)$  defined in (4.16a). Now if we express  $\vec{B}$  in the I-frame we get

$$\begin{aligned} \vec{B} = & |B_3| \sin \beta \sin \omega_z t \hat{1}I + |B_3| \sin \beta \cos \omega_z t \hat{2}I \\ & + |B_3| \cos \beta \hat{3}I . \end{aligned} \quad (5.1)$$

Thus for a given cone half angle  $\beta$ , a coning frequency  $\omega_z$  and a field magnitude  $B_3$ , we can generate  $\vec{B}$  with three orthogonal coils.

For the purpose of this experiment the  $\hat{z}$ -axis or static field coil was chosen to be  $50 \times 10^{-6} \text{ G}$  ( $50 \times 10^{-10} \text{ T}$ ). This will give a Larmor precession of about 1 rad/sec. Two factors which influenced this choice were first the field gradients go up with the field magnitude and second such a slow precession frequency allows for switching of various fields manually.

Next, in order to make the drifts due to the coning motion dominant (and large enough to see on a strip chart recording),  $\beta$  was chosen large enough to give an effect about an order of magnitude greater than earth rate. So choosing  $\beta = 20.35 \text{ deg}$  and  $\gamma B_z = 1.0 \text{ rad/sec}$  gives  $\gamma B_1 = 0.371 \text{ rad/sec}$ . Now Table V-1 shows a comparison of the calculated drift (Eq. 4.17) rate and that predicted by the classical kinematic rectification effect. All of the drift rates shown in Table V-1 should be large compared to any other uncalibrated drift rates. They are also large enough to observe in a time that will be small compared to the expected relaxation time.

#### D. FIELD COIL DESIGN

Since magnetic field uniformity is critical, all four coils (includes the magnetometer pickup coil) are designed in a helmholtz configuration (see Fig. V-3). For this configuration, where each coil has  $N$  turns and the same current,  $I$ , the total magnetic field at any point on the  $z$ -axis is given by

$$B_z(z) = \frac{\mu_0 N I r^2}{2} \left[ \frac{1}{(r^2 + z^2)^{3/2}} + \frac{1}{(r^2 + (z-r)^2)^{3/2}} \right] \quad (5.2)$$

where  $\mu_0$  is the permeability of free space.

Table V-1  
COMPARISON OF CALCULATED DRIFT RATES WITH THOSE  
PREDICTED BY CLASSICAL KINEMATIC RECTIFICATION EFFECTS ALONE

| $\gamma B_3 = 1.067 \text{ rad/sec} \quad \beta = 20.35 \text{ deg}$                                       |   |   |
|--|---|---|
| $\omega_z$<br>(rad/sec)  | Calculated Drift<br>Eq. (4.17)<br>(rad/sec) | Kinematic Rectifica-<br>tion Drift Eq. (4.6)<br>(rad/sec) |
| 0.01   | $6.299 \times 10^{-4}$                      | $6.037 \times 10^{-4}$                                    |
| 0.05   | $3.269 \times 10^{-3}$                      | $3.154 \times 10^{-3}$                                    |
| 0.10   | $6.863 \times 10^{-3}$                      | $6.307 \times 10^{-3}$                                    |
| 0.50   | $5.596 \times 10^{-2}$                      | $3.154 \times 10^{-2}$                                    |
| 0.70   | $1.104 \times 10^{-1}$                      | $4.415 \times 10^{-2}$                                    |
| 0.90   | $2.174 \times 10^{-1}$                      | $5.677 \times 10^{-2}$                                    |
| - 0.01   | $-6.185 \times 10^{-4}$                     | $-6.307 \times 10^{-4}$                                   |
| - 0.05   | $-2.985 \times 10^{-3}$                     | $-3.154 \times 10^{-3}$                                   |
| - 0.10   | $-5.721 \times 10^{-3}$                     | $-6.307 \times 10^{-3}$                                   |
| - 0.50   | $-2.140 \times 10^{-2}$                     | $-3.154 \times 10^{-2}$                                   |
| - 1.00   | $-3.247 \times 10^{-2}$                     | $-6.307 \times 10^{-2}$                                   |
| - 5.00   | $-5.513 \times 10^{-2}$                     | $-3.154 \times 10^{-1}$                                   |
| -10.0  | $-6.034 \times 10^{-2}$                     | $-6.307 \times 10^{-1}$                                   |
| -50.0  | $-6.525 \times 10^{-2}$                     | -3.154  |
| Note: The smallest expected drift is $-6.185 \times 10^{-4} \text{ rad/sec} = -2.126 \text{ deg/minute}$ . |   |   |



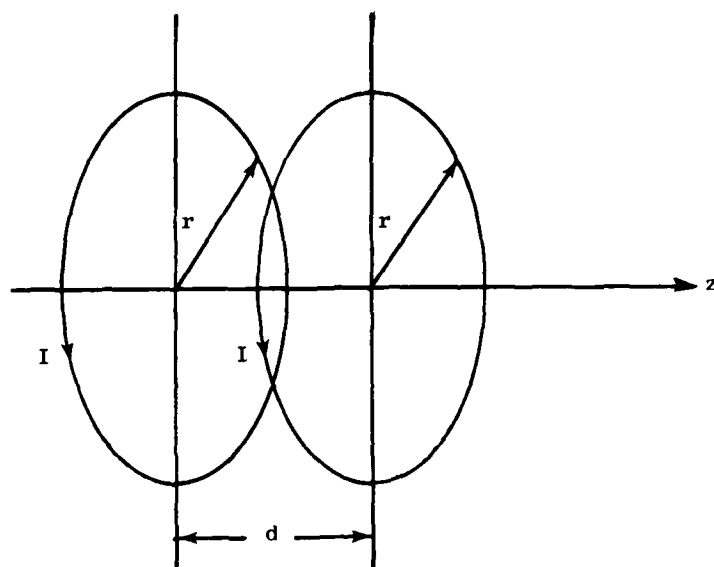


FIG. V-3 HELMHOLTZ COIL CONFIGURATION. Here  $d = r$   
to make

$$\frac{d}{dz} B_z\left(\frac{r}{2}\right) = \frac{d^2}{dz^2} B_z\left(\frac{r}{2}\right) = 0 .$$

It is easy to show from (5.2) that both the first and second derivatives of the field, with respect to  $z$ , vanish at the center ( $z = r/2$ ).

The values for  $\gamma B_z$  and  $\gamma B_1$  were given in the previous section as 1.0 rad/sec and 0.371 rad/sec respectively. Thus the 3G axis coil must produce a steady  $50 \times 10^{-6} \text{G}$  ( $50 \times 10^{-10} \text{T}$ ) field, while the 1G and 2G axis coils must generate peak fields of  $18.199 \times 10^{-6} \text{G}$  ( $18.199 \times 10^{-10} \text{T}$ ). To accomplish this, these coils were designed as specified in Table V-2. Figure V-4 shows the calculated field profile across the sample cell for each coil pair. As mentioned earlier the coil forms are machined out of Macor. After machining the Macor, forms are degreased and processed in an acid bath to remove any possible magnetic contaminants picked up in the machining process. Assembly is performed on a clean bench. Figure V-5 shows the coil form assembly.

Table V-2

FIELD COIL SPECIFICATIONS

| Gyro Axis                        | Diameter<br>(meters) | Number of Turns | Peak Current<br>(amps)    |
|----------------------------------|----------------------|-----------------|---------------------------|
| 1G                               | $4.0 \times 10^{-2}$ | 4               | $10.117 \times 10^{-6}$   |
| 2G                               | $5.2 \times 10^{-2}$ | 5               | $10.521 \times 10^{-6}$   |
| 3G                               | $7.2 \times 10^{-2}$ | 6               | $33.354 \times 10^{-6} *$ |
| * Note this is a steady current. |                      |                 |                           |

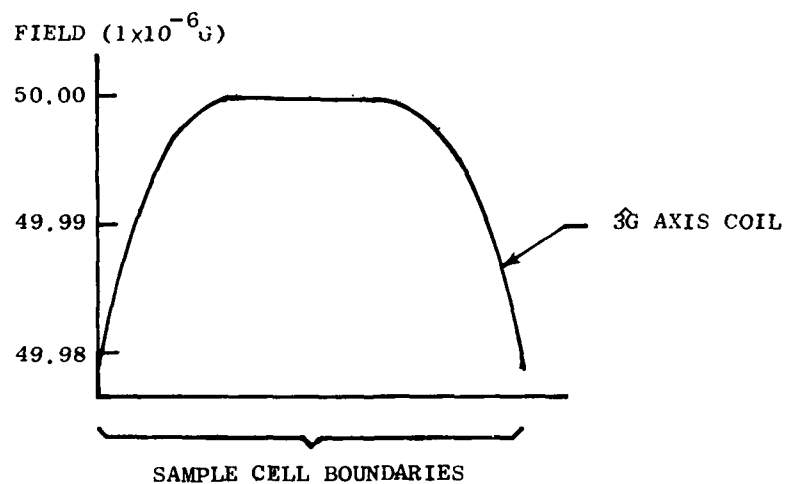
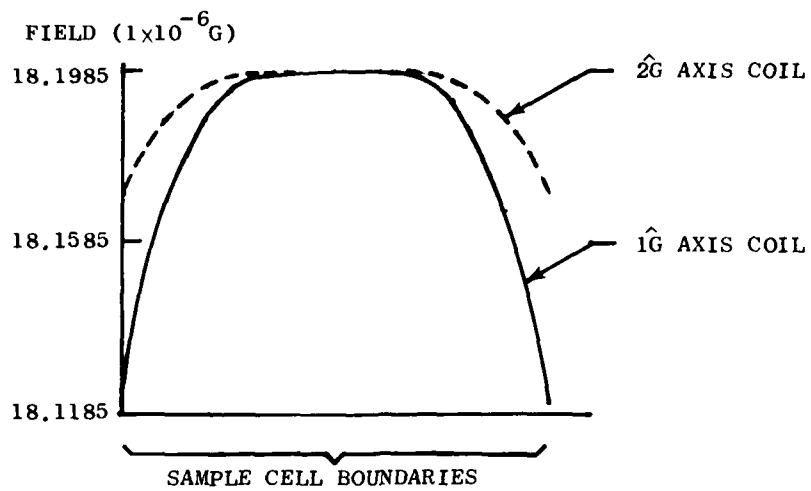


FIG. V-4 AXIAL FIELD PROFILES. Calculated field values along each coil pair axis, over the sample cell boundaries.

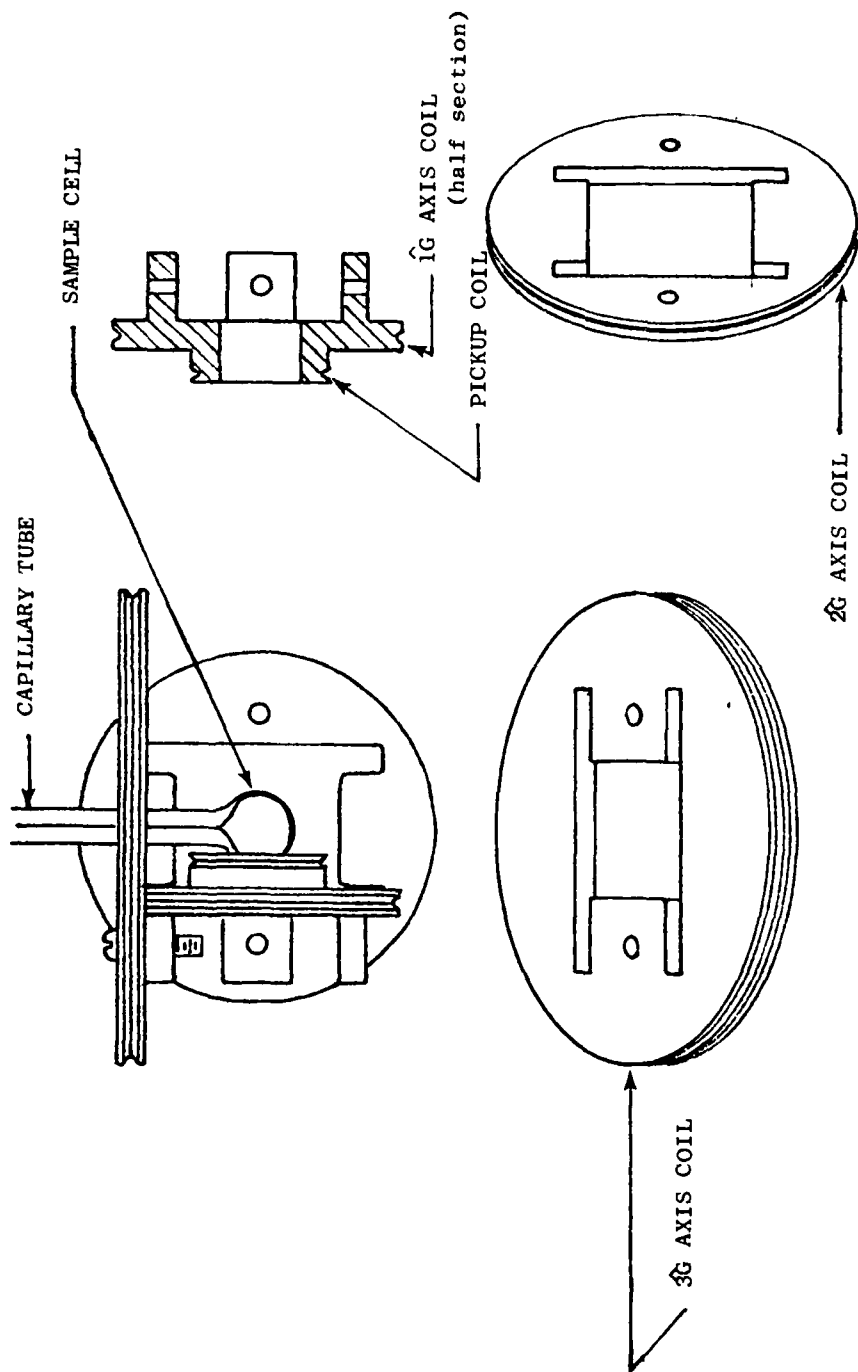


FIG. V-5 COIL FORM ASSEMBLY (full scale)

### E. EXPERIMENTAL PROCEDURE

The basic procedure for running this experiment would be as follows.

- 1) Turn on the  $\hat{3}G$ -axis coils and condense the polarized  $He^3 - He^4$  mixture in the sample cell. At this point the magnetization should be aligned with the applied field.
- 2) Turn off the  $\hat{3}G$ -axis coils and turn on the  $\hat{2}G$ -axis coils at a steady value. At this point  $\vec{M}$  should be precessing about the  $\hat{2}G$ -axis.
- 3) Monitor the precessing  $\vec{M}$  via the magnetometer output. When the magnetometer output indicates a maximum (or minimum), turn off the  $\hat{2}G$ -axis coils and turn on the  $\hat{3}G$ -axis coils. Now  $\vec{M}$  should be precessing about the  $\hat{3}G$ -axis. This is the normal operating condition for the gyro.

The next step is to apply the rotating field. Figure V-6 shows a simple method of generating this rotating field using a TR-20 desktop analog computer. To establish the initial conditions described in the previous chapter, follow this procedure.

- 1) With the analog computer in the reset mode, monitor the magnetometer output. When the magnetometer indicates a maximum, close switch No. 1.
- 2) Continue to monitor the magnetometer output; and, at the next maximum, switch the analog computer to the operate mode.
- 3) To change the direction of  $\omega_z$ , toggle switch No. 2.

The peak current for each coil is determined by the particular combination of initial condition (IC) and scale factor (SF) pots.

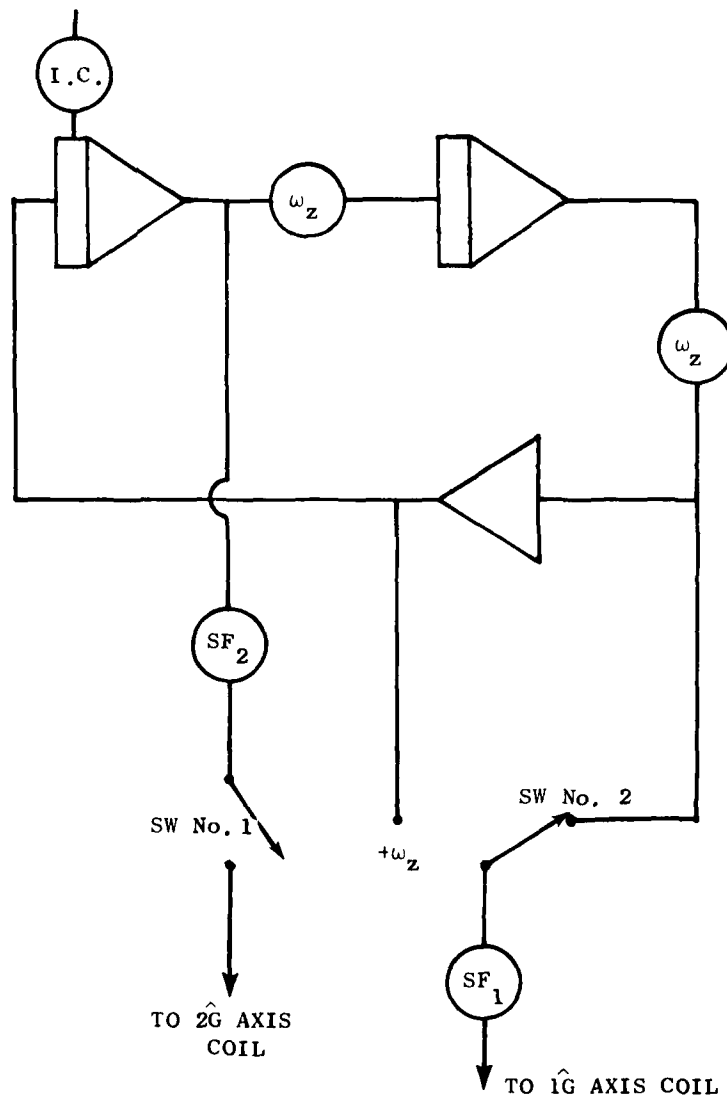


FIG. V-6 TR-20 CIRCUIT TO GENERATE  $B_1$ .

Potentiometers  $\omega_z$  set the coning frequency; Pot. IC sets the amplitude and is used in conjunction with pots  $SF_1$  and  $SF_2$  to determine peak currents in the  $1\hat{G}$  and  $2\hat{G}$  axis field coils.

## Chapter VI

### FIELD GRADIENT EFFECTS

#### A. FIELD GRADIENT SOURCES

Recall that the basis for determining rotations with a  $\text{He}^3$  nuclear gyro is the stability and uniformity of the applied magnetic field. Stability is enhanced by use of superconducting field coils and superconducting magnetic shielding; but we have already noted that our present capabilities do not permit us to trap a perfectly uniform field. We also saw in the previous chapter that the field generated by a helmholtz pair is not perfectly uniform. This latter source of nonuniformity can be reduced by using larger helmholtz coils or going to a higher order helmholtz configuration which would require additional coil pairs to correct for nonuniformity. So if we are willing to pay the price on the field coils, we are limited by the nonuniformity of the trapped field. Based on present accomplishments [Cabrera 1975] we would expect to be able to obtain fields with a linear gradient term of less than  $10^{-8} \text{ G cm}^{-1}$  ( $10^{-10} \text{ T m}^{-1}$ ).

#### B. REDUCTION OF TRANSVERSE RELAXATION TIME

One very significant effect of magnetic field gradients is to reduce the transverse relaxation time,  $T_2$ . Taber [Taber 1977] has covered the theory of this effect in detail, so only the final result and a qualitative explanation are included here. Consider the situation shown in Fig. VI-1. The magnetic field has a linear axial gradient such that

$$\vec{B} = (B_0 + az)\hat{z} \quad (6.1)$$

where  $a$  is the linear gradient coefficient. Since the precession frequency for a given nucleus depends on the local value of the field, the two  $\text{He}^3$  nuclei shown in Fig. VI-1, though initially aligned, are not precessing at the same frequency. If these nuclei remained in their

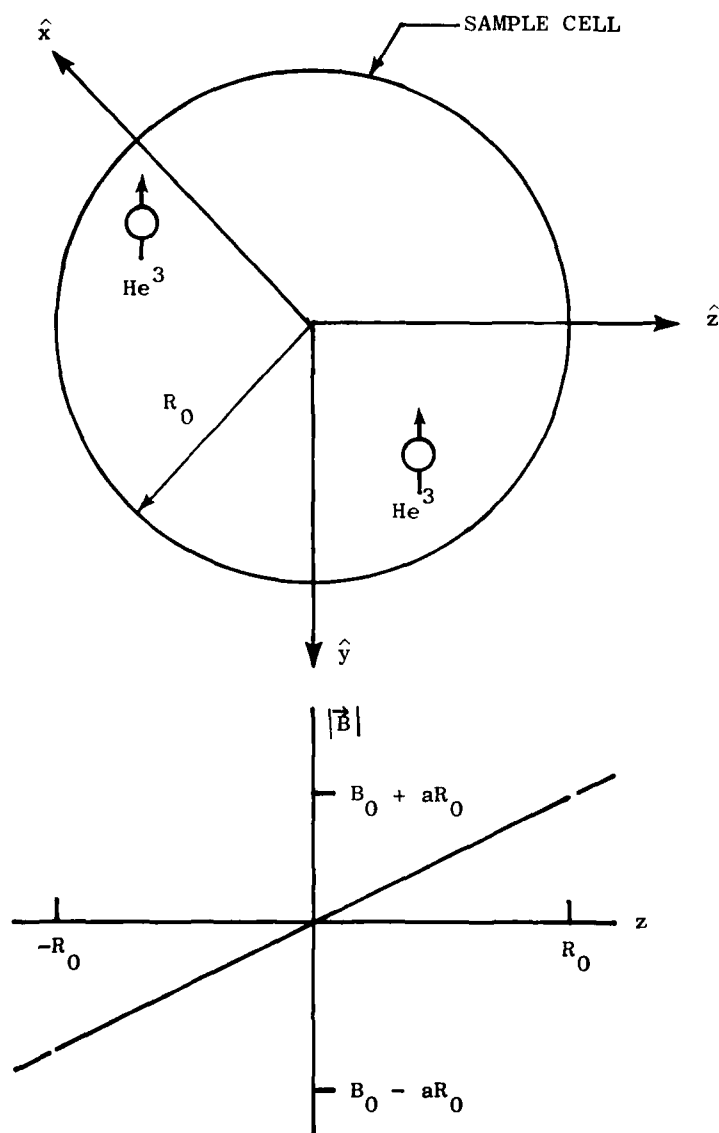


FIG. VI-1 AXIAL FIELD PROFILE ACROSS SAMPLE CELL.

$$\vec{B} = (B_0 + az)\hat{z}.$$



respective positions, then the angle between their spin axes would grow linearly with time. However, the  $\text{He}^3$  nuclei are not stationary, but are continuously diffusing through the sample cell. If, on the average, a given nucleus will spend as much time in one location as any other, then the gradient is averaged out, and the average precession rate is  $\gamma B_0$  rad/sec. Though each will have the same average precession frequency, the two nuclei shown in Fig. VI-1 will have different magnetic field time histories and thus will still become misaligned. The faster they diffuse through the sample cell, though, the shorter will be the time required to average out any differences, and thus the longer will be the time that they maintain close relative alignment.

It is this net alignment of a large number of  $\text{He}^3$  nuclei that produces the signal sensed by the magnetometer. So as the alignment becomes scrambled, the magnetization, and hence the signal decays to zero. The rate of this decay is exponential with a characteristic time,  $T_{2G}$ , given by

$$T_{2G}^{-1} \leq 0.16 \gamma^2 a^2 R_0^4 D^{-1} \quad (6.2)$$

where  $D$  is the  $\text{He}^3$  diffusion coefficient. So to maximize  $T_{2G}$  we would make  $R_0$  very small and  $D$  very large. However, we cannot do this with impunity.  $D$  depends on density and on temperature; and since the field coils, pickup coils and magnetic shields are superconducting we are limited in temperature. Further, if it turns out to be advantageous to coat the sample cell walls with solid hydrogen, then we must maintain the temperature below 8 K. We also have restrictions on the  $\text{He}^3$  density. For a given polarization and volume, the total magnetic flux produced by the sample is proportional to its density. Thus to increase  $D$  by lowering the density would require increasing  $R_0$  to maintain the same signal level. So one must trade off decay rate versus initial magnitude. Then, as we will see in the next two sections, there are other factors which will influence the choices.

Note that this depolarization process, referred to as gradient induced relaxation, affects the transverse but not the longitudinal relaxation time. Since nuclei aligned with the field (or anti-aligned)

do not precess, their alignment is not affected by any axial field gradients. This is one factor which makes the transverse relaxation time generally shorter than the longitudinal relaxation time.

### C. GRADIENT INDUCED g-SENSITIVE DRIFT

In addition to shortening the relaxation time, magnetic field gradients have a more subtle influence on nuclear gyro performance. Should the external environment (e.g., thermal or gravitational) induce a density gradient in the  $\text{He}^3$  which has a component along the field gradient, then the average field seen by the nuclei will no longer be the field,  $B_0$ , at the geometric center of the sample cell. Thus there will be a shift in the average precession rate, which, to the extent that it is neither measured nor corrected, will result in a drift. These effects will be more pronounced in gaseous samples but will also be present in liquid  $\text{He}^3$  -  $\text{He}^4$  solutions.

So let us consider the case of a gaseous sample with an axial field gradient, undergoing a constant acceleration along the field direction. In particular, consider the field given by (6.1) and the acceleration to be in the  $\hat{z}$  direction. Then the  $\text{He}^3$  density will be a function of  $\hat{z}$  and can be determined as follows.

Consider the one-dimensional equation of hydrostatic equilibrium

$$\frac{dP}{dz} = -\rho g . \quad (6.3)$$

Then if we consider the  $\text{He}^3$  to be isothermal

$$P = \rho RT \quad (6.4)$$

and

$$\frac{d\rho}{\rho} = -\frac{g}{RT} dz . \quad (6.5)$$

The quantity  $RT/g$  is commonly referred to as the scale height,  $H_0$ , and we can write

$$\frac{d\rho}{\rho} = -\frac{dz}{H_0} . \quad (6.6)$$

If we integrate over the sample cell from  $z = -R_0$  to  $z$ , we get the density as a function of  $z$  to be

$$\rho(z) = \rho(-R_0) e^{-(z+R_0)/H_0} . \quad (6.7)$$

Now we can compute the average magnetic field seen by the  $\text{He}^3$  nuclei as

$$B_{av} = \frac{\int \rho |\vec{B}| dv}{\int \rho dv} \quad (6.8)$$

where the integrations are carried out over the sample cell volume. Since both  $\vec{B}$  and  $\rho$  are functions only of  $z$  we can rewrite (6.8) as

$$B_{av} = \frac{\int_{-R_0}^{R_0} \rho(-R_0) e^{-(z+R_0)/H_0} (B_0 + az) \pi(R_0^2 - z^2) dz}{\int_{-R_0}^{R_0} \rho(-R_0) e^{-(z+R_0)/H_0} \pi(R_0^2 - z^2) dz} . \quad (6.9)$$

Performing the integrations gives the results

$$B_{av} = B_0 + aR_0 \left[ \frac{e^{-r}(r^2 + 3r + 3) - e^r(r^2 - 3r + 3)}{r[e^{-r}(1+r) - e^r(1-r)]} \right] \quad (6.10)$$

where

$$r = \frac{R_0}{R_0} . \quad (6.11)$$

So if we rewrite (6.10) as

$$B_{av} = B_0 + \delta B \quad (6.12)$$

we see that the result of a constant acceleration is to shift the average magnetic field by  $\delta B$ . This will cause the precession frequency to shift by  $\gamma \delta B$  rad/sec.

We could plot families of curves showing the drift rate vs acceleration level for a number of values of  $R_0$ ,  $a$ , and  $T$ , but it is more convenient to plot a single curve using two nondimensional quantities. These are a normalized drift rate  $\gamma\delta B/\gamma a R_0$ , which represents a fraction of the maximum drift rate due to acceleration and the sample cell radius as a fraction of scale height ( $R_0/H_0$ ). This one curve (Fig. VI-2) contains all the information to determine the g-sensitive drift rate for any set of conditions. Figure VI-2 shows that the drift rate increases with  $g$ ,  $T^{-1}$ , and  $R_0^2$ .

As an example, it is interesting to calculate this effect for the  $\text{He}^3$  nuclear gyro being designed for the electric dipole moment experiment. Assuming a sample cell temperature of 5K,  $R_0$  of  $1.9 \times 10^{-2}$  m,  $1g$ , and a linear field gradient of  $10^{-8} \text{ G-cm}^{-1}$  ( $10^{-10} \text{ T-m}^{-1}$ ), we get

$$H_0 = 1.413 \times 10^3 \text{ m}$$

$$\frac{R_0}{H_0} = 1.345 \times 10^{-5}$$

$$\frac{\gamma\delta B}{\gamma a R_0} = 2.8 \times 10^{-6} \text{ (from Fig. VI-2)}$$

$$\gamma a R_0 = 872 \times 10^{-4} \text{ rad/sec .}$$

Thus the drift rate  $\gamma\delta B$  is  $1.084 \times 10^{-9}$  rad/sec (0.00022 deg/hr). Then, since this effect is linear in acceleration, we get for this device a g-sensitive drift term of 0.00022 deg/h per g. And this is a worst case where both the field gradient and the density gradient are parallel. In general, the g-sensitive drift term will scale as the cosine of the angle between the two gradients.

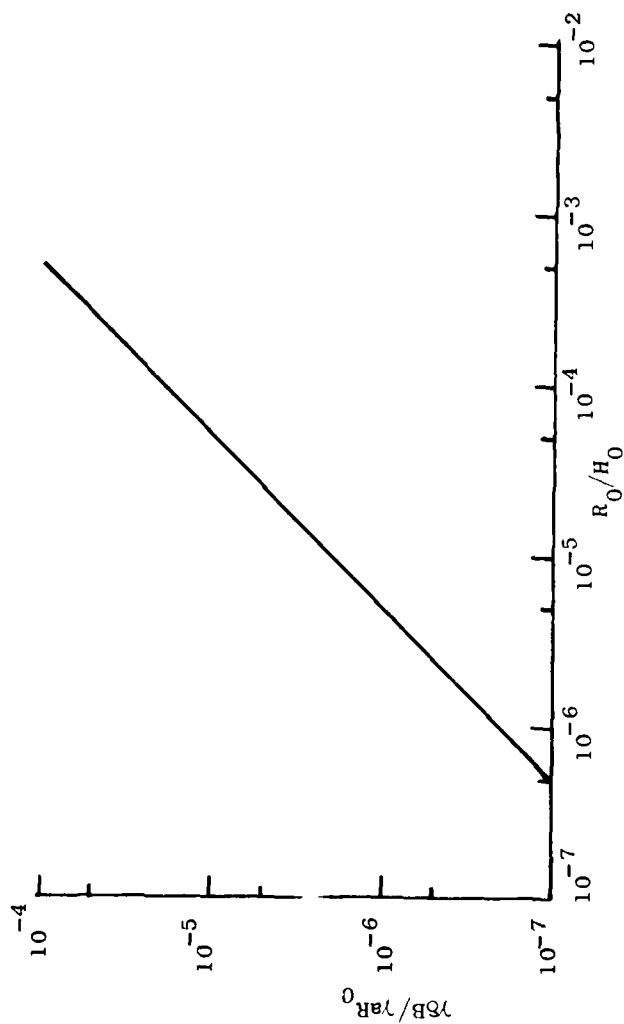


FIG. VI-2 GYRO DRIFT DUE TO CONSTANT ACCELERATION. Drift rate as a fraction of maximum g-sensitive drift versus sample cell size as a fraction of scale height.

#### D. GRADIENT INDUCED TEMPERATURE SENSITIVE DRIFT

Now let us evaluate the effect of a temperature gradient induced density gradient. Again, use Eq. (6.1) for the magnetic field and describe the temperature as

$$T(z) = T_0 + bz \quad (6.13)$$

where  $T_0$  is the temperature at the center of the sample cell and  $b$  is a linear temperature gradient coefficient (assumed in the  $z$ -axis direction to give a worst case drift). Now setting the acceleration to zero, (6.3) gives a constant pressure. Then from (6.7) we get

$$\rho(z) = \frac{\rho_0 T_0}{T_0 + bz} \quad (6.14)$$

where

$$\rho_0 = PR^{-1}T_0^{-1} \quad (6.15)$$

So again with both  $\vec{B}$  and  $\rho$  as functions only of  $z$  we can write (6.8) as

$$B_{av} = \frac{\int_{-R_0}^{R_0} \frac{\rho_0 T_0}{T_0 + bz} \pi(R_0^2 - z^2)(B_0 + az) dz}{\int_{-R_0}^{R_0} \frac{\rho_0 T_0}{T_0 + bz} \pi(R_0^2 - z^2) dz} \quad (6.16)$$

And performing the integrations gives

$$B_{av} = B_0 + aR_0 \left[ \frac{\frac{4}{3}t^{-1} - 2t - \ln\left(\frac{1+t^{-1}}{1-t^{-1}}\right)(1-t^2)}{2 + \ln\left(\frac{1+t^{-1}}{1-t^{-1}}\right)(t^{-1} - t)} \right] \quad (6.17)$$

where  $t$  is the temperature at the center,  $T_0$ , divided by the maximum temperature difference from  $T_0$ ,  $bR_0$  (i.e.  $t = T_0/bR_0$ ).

Rewriting (6.17) as

$$B_{av} = B_0 + \delta B' \quad (6.18)$$

it is again convenient to plot nondimensional quantities  $\gamma \delta B' / \gamma a R_0$  vs  $t^{-1}$  (Fig. VI-3) rather than families of curves.

As an example let us again use the gyro design of the electric dipole moment experiment and calculate how large a temperature gradient can be allowed while keeping the temperature gradient induced drift less than 0.001 deg/hr ( $4.85 \times 10^{-9}$  rad/sec). Using the same values as before, we get

$$\gamma a R_0 = 3.872 \times 10^{-4} \text{ rad/sec}$$

$$\frac{\gamma \delta B'}{\gamma a R_0} = 1.252 \times 10^{-5}$$

$$t^{-1} = \frac{b R_0}{T_0} = 6.4 \times 10^{-4} \text{ (from Fig. VI-3)}$$

$$\frac{R_0}{T_0} = 3.8 \times 10^{-3} \text{ m-K}^{-1}.$$

Thus

$$b = 1.68 \times 10^{-1} \text{ K-m}^{-1}.$$

This would require temperature control of about 6 parts in  $10^4$ .

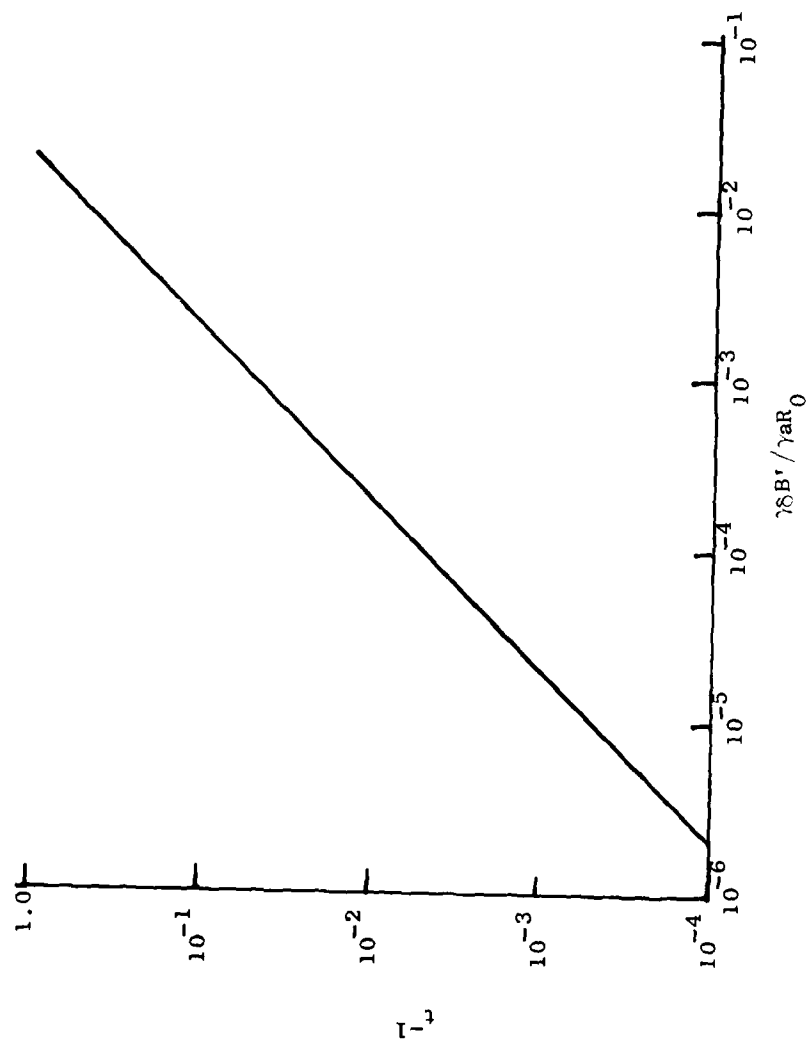


FIG. VI-3 GYRO DRIFT DUE TO TEMPERATURE GRADIENT. Maximum temperature variation from  $T_0$  as a fraction of  $T_0$  ( $T_1$ ) vs drift rate as a fraction of the maximum temperature sensitive drift.



## Chapter VII

### CONCLUSIONS AND RECOMMENDATIONS

#### A. CONCLUSIONS

The mathematical models developed in this research may be used to predict the behavior of a cryogenic  $\text{He}^3$  nuclear gyro in the presence of rotations, vibrations, and magnetic field gradients (i.e., field gradient interactions with acceleration and thermal gradients).

Application of these models to the electric dipole moment gyro showed that thermal gradient control requirements would not be stringent ( $\sim 0.06\%$ ); and sensitivity to acceleration is very small ( $0.00022 \text{ deg/h-g}$ ).

The major problems uncovered through exercising these models relate to oscillatory cross axis rotations. These types of motions introduce drifts through various rectification mechanisms and can lead to a loss of output signal by causing the sample magnetization to align with the applied field. The latter situation can be precluded through the use of additional field coils in the cross axes to reduce cross axis rotation effects; and, if necessary, to torque the sample magnetization away from the applied field direction.

With regard to the rectification mechanisms we find conflicting requirements. Drifts due to high frequency vibrations, that reduce the effective field, are reduced by decreasing the applied field. Cross axis rectification effects, however, are reduced by increasing the applied field. Also, since increasing the applied field increases the precession frequency of the magnetization, increasing the applied field will increase the bandwidth of the gyro and thus increase the effectiveness of the cross axis field coils. One solution to this apparent dilemma would be to generate as large an applied field as practical (field gradients generally increase with field magnitude) and then employ a mechanical mount which would attenuate high frequency cross axis oscillations. The mechanical mount should be notched to severely attenuate vibrations at the resonance frequency.

The experiment discussed in Ch. V allows verification of the frequency dependent of both kinematic and cross axis rate rectification mechanisms by varying the coning frequency. This experiment may be conducted with a relatively simple apparatus; and, by using rotating magnetic fields, no mechanical coning motions are required. The smallest induced drift for this experiment was greater than 2 deg/min. This is easily observed and over an order of magnitude greater than drifts due to other sources.

#### B. RECOMMENDATIONS

There are a number of areas where technological improvements will make the cryogenic  $\text{He}^3$  nuclear gyro more practical. Among these would be development of small size closed cycle cryogenic refrigerators, development of a method to polarize the  $\text{He}^3$  in the sample cell at cryogenic temperature, and development of other cryogenic devices such as accelerometers, gravity gradiometers, and computers that could be packaged with the  $\text{He}^3$  gyro to provide an all cryogenic inertial measurement unit. Development of methods to improve the magnetic field qualities and, in particular, to increase the magnitude of the applied field without producing large gradients will lead directly to improved performance of a  $\text{He}^3$  gyro.

In addition to the experiments planned for both the Macor and fused quartz gyros, it would be highly desirable to perform some experiments to observe cross axis effects. Effective cross axis rate inputs could be applied as fields through the cross axis field coils or by using the  $2\hat{G}$ -axis coil for the applied field and rotating the dewar about the  $3\hat{G}$  axis.

Development of a three orthogonal gyro simulation (preferably with the capability of substituting the actual gyro for one of the simulated gyros) would allow evaluation of various feedback schemes to reduce cross axis effects, as discussed in Chapter III.

The nuclear gyro shows its greatest potential for a practical application in a strapped-down mode. However, before this potential can be realized the cross axis effects must be removed.

## REFERENCES

- Abraham, A. The Principles of Nuclear Magnetism, Oxford Press, 1973.
- Cabrera, Blas, "The Use of Superconducting Shields for Generating Ultra-Low Magnetic Field Regions and Several Related Experiments," Ph.D. Thesis, Dept. of Physics, Stanford University, Stanford, CA., 94305, 1975.
- Cannon, R.H., "Kinematic Drift of Single-Axis Gyroscopes," J. of Applied Mechanics, Paper No. 57-A-72.
- Cohen-Tannoudji Claude, et al., Quantum Mechanics, (Vols. 1 and 2), John Wiley & Sons, New York, NY, 1977.
- Colegrove, F.D., et al., Physics Rev., Vol. 132, pp. 2561, 1963.
- Fairbank, W.M., and Hamilton, W.O., Proc. 10th Int. Conf. on Low Temperature Phys., Vol. IIB, p. 327, 1967.
- Giffard, R.P., J. of Low Temp. Phys., Vol. 6, pp. 533, 1972.
- Kanegsberg, E., et al., "Investigation of Bias Stability and Cross Axis Effects and Brassboard Gyro Conceptual Design for a Nuclear Magnetic Resonance Gyro," Technical Rept., Air Force Avionics Lab., AFAL/RWA, WPAFB, Ohio 45433, No. AFAL-TR-78-1155, Oct. 1979.
- Macek, W.M., et al., "Ring Laser Rotation Rate Sensor," Proc. of the Symposium on Optical Masers, New York, 1963.
- SHE Manufacturer Handbook, SHE Corporation, San Diego, CA., 92121.
- Silver, A.H., Zimmerman, J.E., Phys. Rev., Vol. 157, pp. 317, May 1967.
- Simpson, J.H., et al., "Nuclear Magnetic Resonance Gyro Design and Test Study," Technical Rept., Air Force Avionics Lab., AFAL/RWA, WPAFB, Ohio, 45433, No. AFAL-TR-79-1199, Dec. 1979.
- Taber, M.A., "I: Spin-Lattice Relaxation of Dilute Solutions of Polarized  $\text{He}^3$  in Liquid  $\text{He}^4$  in Low Magnetic Fields at 4K. II: An Analysis of a proposed Cryogenic  $\text{He}^3$  Nuclear Gyroscope and its Application to a Nuclear Electric-Dipole Moment Experiment," Ph.D. Thesis, Dept. of Physics, Stanford University, Stanford, CA, 94305, 1978.
- Zimmerman, J.E., et al., J. of Applied Phys., Vol. 41, No. 4, pp. 1572-1580, March 1970.

END

DATE  
FILMED

7-81

DTIC